Shining light on collective modes in moiré fractional Chern insulators

Nisarga Paul,[1, *] Ahmed Abouelkomsan,[1, *] Aidan Reddy,[1, *] and Liang Fu[1]

[1]*Department of Physics, Massachusetts Institute of Technology, Cambridge, Massachusetts 02139, USA*

We show that collective excitations and optical responses of moiré fractional Chern insulators (FCIs) drastically differ from those of standard fractional quantum Hall (FQH) states in a Landau level. By constructing a variational wavefunction that incorporates the moiré lattice effect, we capture the collective modes in FCIs across a range of crystal momenta including the roton minimum. Interestingly, new collective modes —"fractional excitons"— are found in the long wavelength limit ($\boldsymbol{q} \to 0$) at low energy below the excitation continuum, distinct from the FQH case. Some of these modes are optically active and manifest as sharp peaks in optical conductivity at THz frequency. We further show that intraband optical absorption and spectral weight in twisted MoTe₂ are highly tunable by the displacement field. Our work thus establishes optical spectroscopy as a powerful tool to illuminate the unique collective modes of moiré FCIs.

Introduction— The fractional quantum anomalous Hall (FQAH) effect observed in two-dimensional moiré materials [1–5], despite occurring at zero magnetic field, bears a striking similarity with the fractional quantum Hall (FQH) effect in Landau levels. In the case of twisted transition metal dichalcogenides (tTMDs), this similarity was understood—and even anticipated [6–8]—by the close analogy between flat Chern bands [9] and Landau levels. The FQAH states in these partially filled Chern bands, which may be called moiré fractional Chern insulators (FCIs) [10–12], belong to the same phase as the corresponding FQH states in Landau levels. A natural question is whether these moiré FCIs host new phenomena that go beyond decades-long FQH research.

In this work, we show that the low-energy collective modes and optical response of moiré FCIs are drastically different from those of FQH states. For FCIs in twisted TMDs, we find that intraband collective excitations at zero wavevector $q = 0$ exist below the continuum and are optically active, giving rise to sharp peaks in optical absorption at terahertz frequencies. This is in sharp contrast with FQH states in Landau levels, where all intra-Landau level excitations are optically dark (Kohn's theorem) [13]. We further show using a sum rule that the low-energy spectral weight is highly tunable by the displacement field. Our work suggests low-energy optical spectroscopy as a powerful probe of collective modes in moiré FCIs.

The starting point of our analysis is the continuum model for twisted TMD homobilayers [9]. For one valley (equivalently spin), it reads $H = H_\uparrow + H_C$, with H_C describing Coulomb interactions and

$$H_\uparrow = \frac{\hbar^2 \boldsymbol{k}^2}{2m^*}\sigma_0 + \boldsymbol{J}(\boldsymbol{r}) \cdot \boldsymbol{\sigma} + V(\boldsymbol{r})\sigma_0 \tag{1}$$

where $\{\sigma_0, \boldsymbol{\sigma}\}$ are the identity and Pauli matrices in the layer-pseudospin space. $\boldsymbol{J}(\boldsymbol{r})$ is a layer Zeeman field that includes both interlayer tunneling and layer potential bias, and $V(\boldsymbol{r})$ is a periodic potential, both varying periodically with the moiré period.

As we shall show below, it is conceptually useful to consider the continuum model above in the large-J limit [14–17] under which the layer pseudospin is locally aligned to the Zeeman field, giving rise to the effective Hamiltonian $H = \tilde{H} + H_C$ with

$$\tilde{H} = \frac{(\boldsymbol{p} + eA(\boldsymbol{r}))^2}{2m^*} + \tilde{V}(\boldsymbol{r}) \tag{2}$$

where $A(\boldsymbol{r})$ is a $U(1)$ gauge field representing a periodically varying magnetic field that encloses one flux quantum per unit cell and $\tilde{V}(\boldsymbol{r})$ is a periodic scalar potential. This adiabatic approximation maps moiré bands in twisted TMDs to *periodically modulated* Landau levels. The physical picture is that the spatially varying noncoplanar pseudospin texture gives rise to an emergent magnetic field $\boldsymbol{B}_e(\boldsymbol{r}) = \nabla \times \boldsymbol{A}$ that is proportional to the spin chirality [18].

In the following, we shall analyze neutral excitations of moiré FCIs using both the original model (1) and the adiabatic model (2), and gain a better understanding by comparing the two. In each case, we will consider a single Chern band at fractional filling, and assume throughout this work that the gap to remote bands is much larger than the interaction strength. This allows us to neglect band mixing and focus on low-energy intraband excitations.

Collective modes.— To study collective modes in a moiré FCI, we construct a variational ansatz by acting the density operator on the many-body ground state $|0\rangle$:

$$|\phi_{\boldsymbol{q}}^\alpha\rangle = \sum_{\boldsymbol{G}} c_{\boldsymbol{G}}^\alpha \bar{\rho}_{\boldsymbol{q}+\boldsymbol{G}}|0\rangle \tag{3}$$

where $\boldsymbol{q} \in$ BZ is *crystal momentum*, $\boldsymbol{G}$ is a reciprocal lattice vector, the index α labels different excited states at wavevector $\boldsymbol{q}$, and $\{c_{\boldsymbol{G}}^\alpha\}$ is a set of variational coefficients. Here, $\bar{\rho}_{\boldsymbol{k}} = P\rho_{\boldsymbol{k}}P$ where $\rho_{\boldsymbol{k}} = \sum_i e^{-i\boldsymbol{k}\cdot\boldsymbol{r}_i}$ is the density operator at full momentum $\boldsymbol{k}$ (ranging to infinity) and P is the projection operator onto the underlying Chern band subspace.

Importantly, our ansatz uses a linear combination of density operators at multiple wavevectors that differ by a

reciprocal lattice vector, as allowed by the discrete lattice symmetry. This approach goes beyond the single-mode approximation [19–21], and is crucial to capture the effect from the underlying lattice on the excited states of moiré FCIs, as we shall show below.

The variational energy of Eq. (3) is

$$
\begin{aligned}
\varepsilon_{\boldsymbol{q}}^{\alpha} &= \frac{\langle \phi_{\boldsymbol{q}}^{\alpha}|H - E_0|\phi_{\boldsymbol{q}}^{\alpha}\rangle}{\langle \phi_{\boldsymbol{q}}^{\alpha}|\phi_{\boldsymbol{q}}^{\alpha}\rangle} \\
&= \frac{\sum_{\boldsymbol{G}_1\boldsymbol{G}_2} c_{\boldsymbol{G}_1}^{\alpha*} c_{\boldsymbol{G}_2}^{\alpha} \langle 0|\bar{\rho}_{\boldsymbol{q}+\boldsymbol{G}_1}^{\dagger}[H, \bar{\rho}_{\boldsymbol{q}+\boldsymbol{G}_2}]|0\rangle}{\sum_{\boldsymbol{G}_1\boldsymbol{G}_2} c_{\boldsymbol{G}_1}^{\alpha*} c_{\boldsymbol{G}_2}^{\alpha} \bar{s}(\boldsymbol{q}, \boldsymbol{G}_1, \boldsymbol{G}_2)}
\end{aligned}
\tag{4}
$$

where $\bar{s}(\boldsymbol{q}, \boldsymbol{G}_1, \boldsymbol{G}_2) = \langle 0|\bar{\rho}_{\boldsymbol{q}+\boldsymbol{G}_1}^{\dagger} \bar{\rho}_{\boldsymbol{q}+\boldsymbol{G}_2}|0\rangle$ is the projected static structure factor, and $(H - E_0)|0\rangle = 0$. We also write $\bar{s}(\boldsymbol{q}) \equiv \bar{s}(\boldsymbol{q}, 0, 0)$. The variational coefficients $c_{\boldsymbol{G}}^{\alpha}$ can be found by directly diagonalizing the Hamiltonian in the subspace spanned by $\bar{\rho}_{\boldsymbol{q}+\boldsymbol{G}}|0\rangle$.

If $\boldsymbol{q}$ is a high-symmetry crystal momentum, one expects strong hybridization of degenerate modes that are related by lattice symmetry. It is natural then to use the *lowest star* approximation, restricting to a small set of $\boldsymbol{q} + \boldsymbol{G}$ equal in magnitude to $\boldsymbol{q}$. Assuming this set and the Hamiltonian have C_n symmetry for some n, Eq. (4) can be simplified to

$$
\varepsilon_{\boldsymbol{q}}^{\ell} = \frac{\langle 0|\bar{\rho}_{\boldsymbol{q},\ell}^{\dagger}[H, \bar{\rho}_{\boldsymbol{q},\ell}]|0\rangle}{\langle 0|\bar{\rho}_{\boldsymbol{q},\ell}^{\dagger} \bar{\rho}_{\boldsymbol{q},\ell}|0\rangle}
\tag{5}
$$

where $\bar{\rho}_{\boldsymbol{q},\ell} \equiv \sum_{j=0}^{n-1} e^{2\pi i j\ell/n} \bar{\rho}_{\boldsymbol{q}^{(j)}}$ is a chiral projected density operator with angular momentum ℓ and $\boldsymbol{q}^{(j)} = R_{2\pi/n}^{j}[\boldsymbol{q}]$ are the n-fold rotated momenta.

In the following, we will apply the variational ansatz to three cases: (1) ordinary FQH states, (2) the perturbed Landau levels of Eq. (2), and (3) the twisted TMD homobilayer of Eq. (1).

First, we consider the standard FQH effect in the regime where the Coulomb energy $U_0 = e^2/\epsilon\ell_B$ (with ℓ_B the magnetic length) is small compared to the cyclotron gap $\hbar\omega_c$. In this regime, low-energy collective excitations are associated with intra-LL density fluctuations known as magneto-rotons [19]. They exhibit an energy-momentum dispersion which we schematically show in Fig. 1(a). In this case, continuous translation symmetry reduces the variational ansatz to $|\phi_{\boldsymbol{q}}\rangle = \bar{\rho}_{\boldsymbol{q}}|\text{FQH}\rangle$ and Eq. (4) to the standard single-mode approximation (SMA).

A few features of the magneto-rotons are worth noting for our purposes. First, in the $\nu = \frac{1}{3}$ or $\frac{2}{3}$ FQH states, the magneto-roton dispersion has a minimum at a non-zero wavevector $|\boldsymbol{q}_{\text{min}}|\ell_B \approx 1.5$, while it merges with the continuum in the long wavelength limit ($\boldsymbol{q} \to 0$) as illustrated in Fig. 1(a). Second, while SMA is quite accurate for small momenta up to the roton minimum, its accuracy degrades for larger momenta. The neutral excitation at large q that lies below the continuum corresponds to a
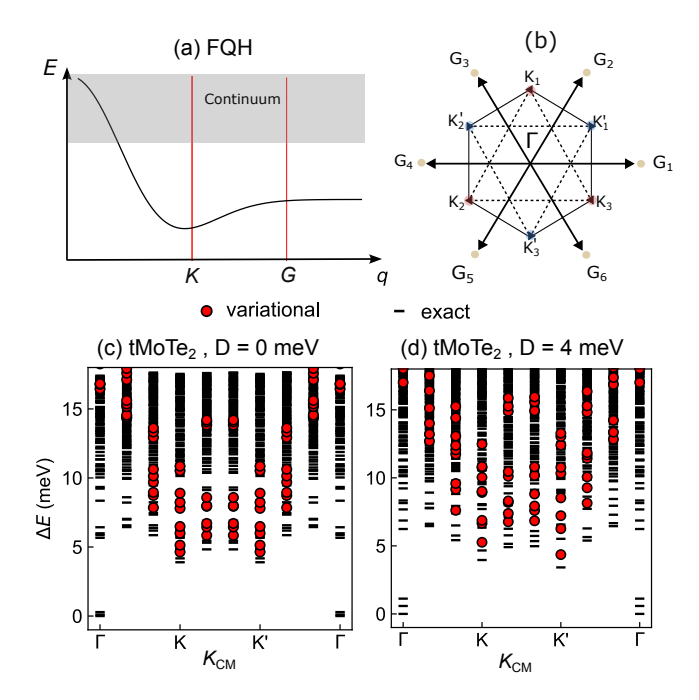

FIG. 1. (a) Schematic illustration of the magneto-roton dispersion of fractional quantum Hall states at $\nu = 1/3$ (or $\nu = 2/3$). The vertical lines denote the K, K' points and first shell reciprocal lattice vectors $\boldsymbol{G}$ (see panel b). (b) Illustration of the folding scheme for the K, K' and Γ points. (c-d) Many-body spectrum of twisted MoTe$_2$ at $n = 2/3$ and twist angle $\theta = 2.5°$ for interlayer potential bias (c) $D = 0$ meV and (d) $D = 4$ meV. $E_0 = -1027.43(-1036.96)$ meV at $D = 0(4)$ meV. The red dots denote the variational energies obtained from the multi-mode approximation (4) while the black lines denote the energies obtained from exact diagonalization on a 27 site cluster (inset of Fig. 2(a)).

fractional quasielectron and quasihole separated by distance $\sim \ell_B^2 q$ [22–26], which may be called a "fractional exciton".

Next, let us consider the case of LLs perturbed by a weak periodic potential, a special case of Eq. (2) with a uniform field. This gives the simplest model for a dispersive Chern band hosting FCIs, provided that the periodic potential is not too strong compared to the Coulomb interaction. Importantly, the periodic potential causes Bragg scattering of collective modes [27, 28]. To calculate the reconstructed excitation spectrum, we write the potential as $\tilde{V}(\boldsymbol{r}) = \sum_{\boldsymbol{G}} \tilde{V}_{\boldsymbol{G}} e^{-i\boldsymbol{G}\cdot\boldsymbol{r}}$, with $|\tilde{V}_{\boldsymbol{G}}| \ll \hbar\omega_c$ and project into the lowest LL. The projected Hamiltonian, including interactions, is

$$
\bar{H} = \sum_{\boldsymbol{G}} \tilde{V}_{\boldsymbol{G}} \bar{\rho}_{\boldsymbol{G}} + \frac{1}{2} \sum_{\boldsymbol{q}} U(\boldsymbol{q}) : \bar{\rho}_{\boldsymbol{q}}^{\dagger} \bar{\rho}_{\boldsymbol{q}} :
\tag{6}
$$

where $\bar{\rho}_{\boldsymbol{q}}$ is the lowest LL-projected density operator and $U(\boldsymbol{q})$ is an interaction of strength U_0. For concreteness, we choose a D_6-symmetric potential enclosing one flux quantum per unit cell with six harmonics: $\tilde{V}_{\boldsymbol{G}} = -V_0$ for

$\boldsymbol{G}_i = \frac{4\pi}{\sqrt{3}a_0}[\cos 2\pi(i-1)/3, \sin 2\pi(i-1)/3]$ for $i = 1, \ldots, 6$ where $\sqrt{3}a_0 = 4\pi\ell_B^2$.

The Bragg scattering of magneto-roton modes by the periodic potential is captured by our variational ansatz Eq. (3), which is a linear combination of excited states at wavevectors $\boldsymbol{q} + \boldsymbol{G}$ as shown by the momentum folding scheme in Fig. 1(b). This can be viewed as a natural generalization of the SMA for FQH liquids to FCIs with discrete translation symmetry. In the Supplemental Material [29], we show how the variational energy can be expressed in terms of the structure factor and ground-state expectation value of $\bar{\rho}_{\boldsymbol{G}}$.

Furthermore, if $V_0 \ll U_0$, the variational energy of excited states can be directly expressed in terms of FQH ground-state expectation values. For instance, to leading order in V_0 the energies of the modes at the K point of the Brillouin zone (BZ), which we refer to as K-rotons, take the form

$$\varepsilon_K^\ell = \Delta_K - \frac{|V_0|}{\bar{s}_0(K)}(S_3 e^{i2\pi\ell/3} + c.c.) \qquad (7)$$

where ℓ labels C_3-angular momentum, Δ_K is the energy of the FQH magneto-roton at wavevector K, and S_3 is three-density correlator defined as:

$$S_3 = \langle \bar{\rho}_{-K_1} \bar{\rho}_{K_1 - K_2} \bar{\rho}_{K_2} \rangle, \qquad (8)$$

where the expectation value is taken in the FQH ground state in the absence of periodic potential. We note that S_3 could in principle be evaluated for a model wavefunction (such as Laughlin) using Monte Carlo [30].

Finally, we turn to the moiré system twisted MoTe$_2$ (tMoTe$_2$), which hosts an FCI with threefold rotational symmetry. Indeed, in the adiabatic limit of Eq. (2), this model maps onto the perturbed Landau level model with the periodic potential enclosing one flux quantum per unit cell. In contrast to the previous case, the variational energies must be evaluated numerically. We perform band-projected exact diagonalization (at hole filling $n = 2/3$ of the $C = 1$ miniband at twist angle $\theta = 2.5°$ and displacement field D [31]), and compare the results with variational energies obtained by diagonalizing the Hamiltonian in the span of all states $\bar{\rho}_{\boldsymbol{q}+\boldsymbol{G}}|\mathrm{GS}_i\rangle$ satisfying $|\boldsymbol{q} + \boldsymbol{G}| \leq \frac{4\pi}{\sqrt{3}a_0}$ where i labels the three quasi-degenerate ground states.

Remarkably, we find that the variational ansatz nicely captures the low-lying excitations near the K and K' points as shown in Fig. 1(c,d). At zero displacement field $D = 0$, $C_{2y}\mathcal{T}$ symmetry relates the K and K' moiré center-of-mass crystal momentum sectors in a fixed valley, enforcing degeneracy between these sectors' many-body spectra. A nonzero D breaks C_{2y} symmetry, thus lifting the K/K' degeneracy as apparent in Fig. 1(d). In particular, the roton minimum softens more strongly at K' than K. Our variational approach succeeds in reproducing this trend.

The success of our variational ansatz near K, K' in tMoTe$_2$ can be qualitatively understood by the adiabatic mapping to perturbed FQH. As illustrated in Fig. 1(a), the K and K'-rotons are derived from magneto-roton modes with $q\ell_B = |K|\ell_B = \frac{2\sqrt{\pi}}{3^{3/4}} \approx 1.6$, which is close to the magneto-roton minimum of the unperturbed FQH liquids (Fig.1(a)) where the SMA is quite accurate. Moreover, Bragg scattering hybridizes magneto-roton modes at K_1, K_2 and K_3, giving rise to three non-degenerate roton modes at the K point in moiré BZ, and likewise for K'.

In contrast with the K-rotons, the collective modes at Γ are poorly captured by the variational ansatz. Figs. 1(c,d) show that the lowest excited states from exact diagonalization at Γ are isolated from the continuum and considerably lower in energy than the variational states. This discrepancy is once again consistent with the mapping to FQH, see Fig. 1(a); variational states at Γ are linear combinations of modes at $\boldsymbol{G}_i$ with $|\boldsymbol{G}_i|\ell_B \approx 2.7$, where the SMA breaks down and collective excitations are better described as quasielectron-quasihole pairs, or *fractional excitons*.

Based on the mapping to perturbed FQH, we expect that the low-energy neutral excitations of tTMD at Γ shown in Fig. 1(c,d) are fractional excitons, analogous to their FQH counterpart at momentum $\boldsymbol{G}$ (which folds back to Γ). A particularly interesting possibility is that these fractional excitons may exist at energies *below* the excitation continuum. Indeed, this scenario is expected to occur when our system maps to *weakly* perturbed FQH and is consistent with the exact diagonalization data shown in Figs. 1(c,d), as we elaborate in the Supplemental Material [29]. The nature of low-energy neutral excitations at Γ are of great interest as they may affect the optical response of the system $\sigma(\boldsymbol{q} \to 0, \omega)$. Although our variational ansatz based on SMA becomes inaccurate here, alternative approaches (e.g., based on composite fermion wavefunctions) [24, 25] may better capture fractional excitons.

Low-frequency optical absorption.— It is well-known that the intra-LL excitations of FQH states have a vanishing dipole coupling to light in the absence of disorder [13]. This is because a uniform electric field only couples to electrons' center of mass, which decouples from other degrees of freedom and has zero intra-LL matrix elements. As a result, optical absorption occurs only at the cyclotron frequency, leaving low-energy collective modes of FQH states optically dark.

In contrast, moiré FCI states only have discrete translation symmetry to which Kohn's theorem does not apply. Thus, a direct coupling between light and $\boldsymbol{q} = 0$ collective excitations with angular momentum $\ell = \pm 1$ is allowed by symmetry. In particular, low-energy fractional excitons may be isolated from the continuum and thus undamped, raising an interesting question of whether they are optically active and can be detected as sharp

peaks in the optical conductivity at low frequency.

Indeed, our calculations of the optical response to circularly polarized light in the many-body ground state of twisted MoTe$_2$ a reveal sharp and prominent peaks at frequencies that correspond to low-lying chiral modes ($\ell = \pm 1$) at Γ, which are further enhanced by displacement fields [29].

To better understand the low-frequency optical response, we derive an intraband f-sum rule for the low-energy optical spectral weight for an FCI formed in an isolated Chern band separated from remote bands by a large gap Δ. In particular, we relate the low-energy spectral weight to a simple ground-state expectation value.

To derive this sum rule, we first perform a Schrieffer-Wolff transformation—a *unitary* transformation U—to decouple the low-energy and high-energy subspace by eliminating the off-diagonal matrix elements (i.e., interband terms):

$$\tilde{H} = UHU^{-1} = \tilde{H}_1 + \tilde{H}_2 \tag{9}$$

where $P\tilde{H}_1 P = \tilde{H}_1$ is the low-energy Hamiltonian acting on a low-energy subspace specified by the projection operator P, and $P_\perp \tilde{H}_2 P_\perp = \tilde{H}_2$ with $P_\perp = I - P$ associated with the high-energy subspace.

To compute the optical conductivity, we find it convenient to relate it to the dynamical structure factor through the continuity equation and fluctuation-dissipation theorem (a thorough discussion for Coulomb systems can be found in Ref. [32]):

$$S(\boldsymbol{q}, \omega) = \frac{\hbar A}{\pi e^2} \frac{q_a q_b}{\omega} \operatorname{Re} \sigma_{ab}(\boldsymbol{q}, \omega). \tag{10}$$

where A is the system area, and the dynamical structure factor is defined as:

$$\begin{aligned} S(\boldsymbol{q}, \omega) &= \sum_{n \neq 0} \delta\left(\omega - \omega_{n0}\right)|\langle n|\rho_{\boldsymbol{q}}|0\rangle|^2 \\ &= \sum_{n \neq 0} \delta\left(\omega - \omega_{n0}\right)|\langle \tilde{n}|\tilde{\rho}_{\boldsymbol{q}}|\tilde{0}\rangle|^2. \end{aligned} \tag{11}$$

where n labels the many-body eigenstate with energy $\hbar\omega_n$ and $\omega_{n0} = \omega_n - \omega_0$ and $\rho_{\boldsymbol{q}}$ is the density operator. In the second equality, we have rewritten S in terms of the many-body eigenstates $|\tilde{n}\rangle \equiv U|n\rangle$ for the transformed Hamiltonian $\tilde{H}$, and $\tilde{\rho}_{\boldsymbol{q}} = U\rho_{\boldsymbol{q}}U^{-1}$.

As $\tilde{H}$ decomposes into low- and high-energy parts, the structure factor is naturally composed of an intraband part that only involves low-energy eigenstates denoted as $|l\rangle$ and an interband part that involves matrix elements between the ground state and high-energy eigenstates denoted as $|h\rangle$,

$$\begin{aligned} S(\boldsymbol{q}, \omega) &= \sum_{l \neq 0} \delta\left(\omega - \omega_{l0}\right)|\langle \tilde{l}|\tilde{\rho}_{\boldsymbol{q}}|\tilde{0}\rangle|^2 \\ &+ \sum_{h} \delta\left(\omega - \omega_{h0}\right)|\langle \tilde{h}|\tilde{\rho}_{\boldsymbol{q}}|\tilde{0}\rangle|^2 \\ &\equiv S^L(\boldsymbol{q}, \omega) + S^H(\boldsymbol{q}, \omega), \end{aligned} \tag{12}$$

with $P|\tilde{l}\rangle = |\tilde{l}\rangle$ and $P_\perp|\tilde{h}\rangle = |\tilde{h}\rangle$. Following Eq. (10), the optical conductivity can be similarly decomposed: $\sigma = \sigma^L + \sigma^H$. In particular, we shall focus on the structure factor and optical conductivity at low frequency, which are dominated by the intraband contributions as captured by the low-energy Hamiltonian $\tilde{H}_1$ [33].

We define the intraband optical spectral weight as

$$W = \int_0^\infty d\omega \, \operatorname{Re} \sigma_{aa}^L(\omega) \tag{13}$$

From Eq. (10) it follows that

$$\begin{aligned} W &= \frac{\pi e^2}{\hbar A} \lim_{q \to 0} \frac{1}{q^2} \sum_{l \neq 0} |\langle \tilde{l}|\tilde{\rho}_{\boldsymbol{q}}|\tilde{0}\rangle|^2 \omega_{l0} \\ &= \frac{\pi e^2}{2\hbar^2 A} \lim_{q \to 0} \frac{1}{q^2} \langle \tilde{0}|[\tilde{\rho}_{\boldsymbol{q}}^{L\dagger}, [\tilde{H}_1, \tilde{\rho}_{\boldsymbol{q}}^L]]|\tilde{0}\rangle \end{aligned} \tag{14}$$

where $\tilde{\rho}^L \equiv P\tilde{\rho}P$ is the density operator projected onto the low-energy subspace.

For our system, the isolated Chern band defines a low-energy subspace, separated by a band gap Δ to remote bands. The corresponding Schrieffer-Wolff transformation can be carried out perturbatively in λ/Δ: $U = I + \mathcal{O}(\lambda/\Delta)$, where $\lambda H' \equiv PHP_\perp + P_\perp HP$ is the interband part of Coulomb interaction with interaction strength λ. To the zeroth-order approximation in λ/Δ, we have $U \approx I$ and $|\tilde{0}\rangle \approx |0\rangle$ is the ground state of band-projected Hamiltonian $\bar{H} \equiv PHP \approx \tilde{H}_1$. Then, the low-energy optical spectral weight simplifies to

$$W = \frac{\pi e^2}{\hbar^2 A} \lim_{q \to 0} \frac{1}{q^2} F(\boldsymbol{q}) \tag{15}$$

with

$$F(\boldsymbol{q}) \equiv \frac{1}{2} \langle 0|[\bar{\rho}_{\boldsymbol{q}}^\dagger, [\bar{H}, \bar{\rho}_{\boldsymbol{q}}]]|0\rangle \tag{16}$$

where $\bar{H}$ and $\bar{\rho}$ the are band-projected Hamiltonian and density operator respectively. Alternatively, the right-hand side of Eq. (15) can be expressed using electron position operator [33], which is well defined for systems with open boundary conditions.

As before, we apply this to the three cases of (1) ordinary FQH states, (2) perturbed Landau levels, and (3) twisted TMD homobilayers. In the case of ordinary Landau levels, only the projected interactions $H_C = \frac{1}{2} \sum_{\boldsymbol{q}} U(\boldsymbol{q}) \bar{\rho}_{\boldsymbol{q}}^\dagger \bar{\rho}_{\boldsymbol{q}}$ remain. We may write

$$F(\boldsymbol{q}) = \frac{1}{2} \sum_{\boldsymbol{q}'} U(\boldsymbol{q}') f_{\boldsymbol{q}'}^{\boldsymbol{q}} \left(f_{\boldsymbol{q}}^{\boldsymbol{q}'} \bar{s}(\boldsymbol{q} + \boldsymbol{q}') + f_{-\boldsymbol{q}}^{\boldsymbol{q} + \boldsymbol{q}'} \bar{s}(\boldsymbol{q}') \right)$$

using the GMP algebra $[\bar{\rho}_{\boldsymbol{q}}, \bar{\rho}_{\boldsymbol{q}'}] = f_{\boldsymbol{q}}^{\boldsymbol{q}'} \bar{\rho}_{\boldsymbol{q}+\boldsymbol{q}'}$ where $f_{\boldsymbol{q}}^{\boldsymbol{q}'} = 2ie^{\boldsymbol{q} \cdot \boldsymbol{q}' \ell_B^2/2} \sin(\boldsymbol{q} \wedge \boldsymbol{q}' \ell_B^2/2)$. Using parity symmetry, it follows $F(\boldsymbol{q})$ vanishes to order q^4 [19, 29], and hence $W = 0$ in this case, which is also consistent with Kohn's theorem.
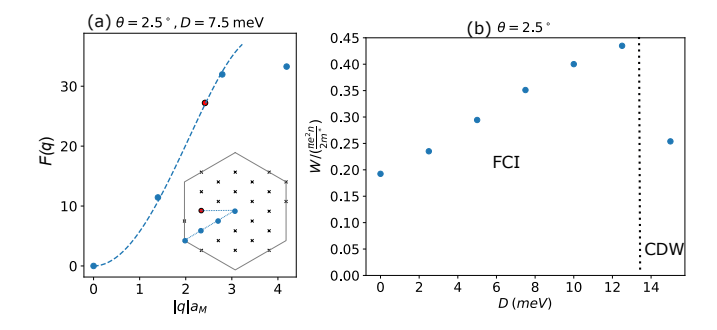
FIG. 2. (a) $F(\boldsymbol{q})$ (equation (16)) calculated for twisted $MoTe_2$ at $n = 2/3$, twist angle $\theta = 2.5°$ and displacement field $D = 7.5$ meV. The inset shows the finite-size cluster along with the cut used in the plot. The data is fitted to a function of the form $F(\boldsymbol{q}) = c_1|\boldsymbol{q}|^2 + c_2|\boldsymbol{q}|^4$ then c_1 is extracted to calculate W (equation (14)). (b) Intraband optical weight W (in units of $\pi e^2 n/(2m^*)$ where n is the density and $m^* = 0.62m_e$ is the effective mass) as a function of displacement field at $\theta = 2.5°$.

In the case of Landau levels perturbed by a periodic potential, the projected Hamiltonian is $\bar{H} = \sum_{\boldsymbol{G}} \tilde{V}_{\boldsymbol{G}}\bar{\rho}_{\boldsymbol{G}} + H_C$. The contribution from H_C vanishes as above, and employing the GMP algebra then yields [28, 34]

$$W = \frac{\pi e^2}{2\hbar^2 A} \sum_{\boldsymbol{G}} \left(-\tilde{V}_{\boldsymbol{G}} \cdot \rho(\boldsymbol{G})\right) (\hat{q} \wedge \boldsymbol{G}\ell_B^2)^2 \qquad (17)$$

where $\rho(\boldsymbol{G}) \equiv \langle 0|\bar{\rho}_{\boldsymbol{G}}|0\rangle = \langle 0|\rho_{\boldsymbol{G}}|0\rangle$ is the Fourier component of the charge density in the *exact* ground state $|0\rangle$ of $\bar{H}$. It is important to note that $\rho(\boldsymbol{G})$ is generally nonzero because of the periodic potential, leading to nonzero intraband spectral weight $W > 0$.

For a generic Chern band such as the bands of twisted $MoTe_2$, it is difficult to compute W analytically. However, we can still evaluate W using the many-body ground state obtained from band-projected exact diagonalization. In Fig. 2(a), we evaluate $F(\boldsymbol{q})$ in the $n = 2/3$ many-body ground state of twisted $MoTe_2$ at $\theta = 2.5°$ and $D = 7.5$ meV. As clearly shown, we observe that $F(\boldsymbol{q})$ scales as $\boldsymbol{q}^2$ implying that W is finite. The finiteness of W extends to a wide range of twist angles [29], demonstrating the robust existence of low-frequency optical absorption, in contrast to recent studies [21, 35].

Remarkably, we find that the low-frequency optical absorption is highly tunable with displacement field D (Fig. 2(b)). As D increases, we observe increasing spectral weight in the FCI phase, consistent with the reduced similarity between the underlying Chern band and the lowest Landau level. We also observe an abrupt decrease in spectral weight as the system undergoes a phase transition to a charge density wave at large D [36, 37].

Discussion.— Our findings suggest new directions for optical experiments on moiré FCIs. The *chiral* fractional exciton modes of tTMDs, with angular momentum $\ell = \pm 1$ and at a few meV excitation energy, can be probed directly using terahertz (THz) spectroscopy, or indirectly

using inelastic Raman scattering (note that $\ell = \pm 1 = \mp 2$ mod 3). Remarkably, our numerical results show that the intraband optical spectral weight can comprise $20 - 40\%$ of the full spectral weight $\pi e^2 n/2m^*$, which is the sum of intraband and interband contributions. We further predict that the intraband optical absorption increases with D field, which can either be observed directly at low frequencies or indirectly at higher frequencies as a *decrease* in the interband optical absorption with D.

In addition to magnetorotons, FQH states also host chiral graviton modes at small $\boldsymbol{q}$ [38–40], which can be probed by Raman scattering [41]. We emphasize that such graviton modes [21, 42, 43] will not be the lowest energy excited states in twisted $MoTe_2$ due to the existence of fractional excitons states that are lower in energy. In the supplemental material [29], we provide numerical evidence that chiral gravitons in periodically modulated LLs are optically active, and leave its detailed study to the future.

While we have focused on the spin-polarized FCIs at $\nu = 1/3$ and $\nu = 2/3$, our variational approach carries over to the FCI analogs of other Jain sequence states, even-denominator non-Abelian FCIs [44–47], non-Abelian spin Hall insulators at $\nu = 3$ [48], and potentially composite Fermi liquids [49–52]. Based on our intraband optical sum rule Eq. 15, we expect nonzero intraband optical absorption to occur in all of these states as well. Other interesting future directions in the study of FCI excitations include the condensation of K-rotons leading to a fractional quantum anomalous Hall crystal [53], excitons of composite fermions, and extensions to lattice FCIs and higher topological bands.

* These authors contributed equally.
[1] J. Cai, E. Anderson, C. Wang, X. Zhang, X. Liu, W. Holtzmann, Y. Zhang, F. Fan, T. Taniguchi, K. Watanabe, et al., Signatures of fractional quantum anomalous hall states in twisted mote2, Nature **622**, 63 (2023).
[2] H. Park, J. Cai, E. Anderson, Y. Zhang, J. Zhu, X. Liu, C. Wang, W. Holtzmann, C. Hu, Z. Liu, et al., Observation of fractionally quantized anomalous hall effect, Na-

ture **622**, 74 (2023).

[3] Y. Zeng, Z. Xia, K. Kang, J. Zhu, P. Knüppel, C. Vaswani, K. Watanabe, T. Taniguchi, K. F. Mak, and J. Shan, Thermodynamic evidence of fractional chern insulator in moiré mote2, Nature **622**, 69 (2023).

[4] F. Xu, Z. Sun, T. Jia, C. Liu, C. Xu, C. Li, Y. Gu, K. Watanabe, T. Taniguchi, B. Tong, et al., Observation of integer and fractional quantum anomalous hall effects in twisted bilayer mote 2, Physical Review X **13**, 031037 (2023).

[5] Z. Lu, T. Han, Y. Yao, A. P. Reddy, J. Yang, J. Seo, K. Watanabe, T. Taniguchi, L. Fu, and L. Ju, Fractional quantum anomalous Hall effect in multilayer graphene, Nature **626**, 759 (2024).

[6] T. Devakul, V. Crépel, Y. Zhang, and L. Fu, Magic in twisted transition metal dichalcogenide bilayers, Nature communications **12**, 6730 (2021).

[7] H. Li, U. Kumar, K. Sun, and S.-Z. Lin, Spontaneous fractional chern insulators in transition metal dichalcogenide moiré superlattices, Physical Review Research **3**, L032070 (2021).

[8] V. Crépel and L. Fu, Anomalous hall metal and fractional chern insulator in twisted transition metal dichalcogenides, Physical Review B **107**, L201109 (2023).

[9] F. Wu, T. Lovorn, E. Tutuc, I. Martin, and A. MacDonald, Topological insulators in twisted transition metal dichalcogenide homobilayers, Physical review letters **122**, 086402 (2019).

[10] A. Abouelkomsan, Z. Liu, and E. J. Bergholtz, Particle-hole duality, emergent fermi liquids, and fractional chern insulators in moiré flatbands, Physical review letters **124**, 106803 (2020).

[11] P. J. Ledwith, G. Tarnopolsky, E. Khalaf, and A. Vishwanath, Fractional chern insulator states in twisted bilayer graphene: An analytical approach, Physical Review Research **2**, 023237 (2020).

[12] C. Repellin and T. Senthil, Chern bands of twisted bilayer graphene: Fractional Chern insulators and spin phase transition, Physical Review Research **2**, 023238 (2020).

[13] W. Kohn, Cyclotron Resonance and de Haas-van Alphen Oscillations of an Interacting Electron Gas, Phys. Rev. **123**, 1242 (1961).

[14] N. Paul, Y. Zhang, and L. Fu, Giant proximity exchange and flat chern band in 2d magnet-semiconductor heterostructures, Science Advances **9**, eabn1401 (2023).

[15] N. Morales-Durán, N. Wei, J. Shi, and A. H. MacDonald, Magic angles and fractional chern insulators in twisted homobilayer transition metal dichalcogenides, Phys. Rev. Lett. **132**, 096602 (2024).

[16] D. Zhai and W. Yao, Theory of tunable flux lattices in the homobilayer moiré of twisted and uniformly strained transition metal dichalcogenides, Physical Review Materials **4**, 094002 (2020).

[17] J. Shi, N. Morales-Durán, E. Khalaf, and A. MacDonald, Adiabatic approximation and aharonov-casher bands in twisted homobilayer transition metal dichalcogenides, Physical Review B **110**, 035130 (2024).

[18] P. Bruno, V. Dugaev, and M. Taillefumier, Topological hall effect and berry phase in magnetic nanostructures, Physical review letters **93**, 096806 (2004).

[19] S. Girvin, A. MacDonald, and P. Platzman, Magnetoroton theory of collective excitations in the fractional quantum hall effect, Physical Review B **33**, 2481 (1986).

[20] C. Repellin, T. Neupert, Z. Papić, and N. Regnault, Single-mode approximation for fractional Chern insulators and the fractional quantum Hall effect on the torus, Physical Review B **90**, 045114 (2014).

[21] X. Shen, C. Wang, X. Hu, R. Guo, H. Yao, C. Wang, W. Duan, and Y. Xu, Magnetorotons in moir\'e fractional chern insulators, arXiv preprint arXiv:2412.01211 (2024).

[22] R. Laughlin, Excitons in the fractional quantum hall effect, Physica B+ C **126**, 254 (1984).

[23] F. D. M. Haldane and E. H. Rezayi, Finite-size studies of the incompressible state of the fractionally quantized hall effect and its excitations, Physical review letters **54**, 237 (1985).

[24] R. Kamilla, X. Wu, and J. Jain, Excitons of composite fermions, Physical Review B **54**, 4873 (1996).

[25] B. Yang, Z.-X. Hu, Z. Papić, and F. D. M. Haldane, Model Wave Functions for the Collective Modes and the Magnetoroton Theory of the Fractional Quantum Hall Effect, Phys. Rev. Lett. **108**, 256807 (2012).

[26] T. Jolicoeur, Shape of the magnetoroton at $\nu = 1/3$ and $\nu = 7/3$ in real samples, Phys. Rev. B **95**, 075201 (2017).

[27] I. V. Kukushkin, J. H. Smet, V. W. Scarola, V. Umansky, and K. von Klitzing, Dispersion of the excitations of fractional quantum hall states, Science **324**, 1044 (2009).

[28] F. Wu and A. MacDonald, Moiré assisted fractional quantum hall state spectroscopy, Physical Review B **94**, 241108 (2016).

[29] See Supplemental Material for details about roton folding in crystalline systems, the variational ansatz introduced in the main text, low-freqeuency optical absorption, evidence for fractional excitons and optical conductivity calculations in periodically modulated Landau levels and twisted MoTe₂.

[30] R. Morf and B. I. Halperin, Monte Carlo evaluation of trial wave functions for the fractional quantized Hall effect: Disk geometry, Phys. Rev. B **33**, 2221 (1986).

[31] A. P. Reddy, F. Alsallom, Y. Zhang, T. Devakul, and L. Fu, Fractional quantum anomalous Hall states in twisted bilayer MoTe₂ and WSe₂, Phys. Rev. B **108**, 085117 (2023).

[32] Y. Onishi and L. Fu, Quantum weight: A fundamental property of quantum many-body systems, arXiv 10.48550/arXiv.2406.06783 (2024), 2406.06783.

[33] D. Mao and D. Chowdhury, Diamagnetic response and phase stiffness for interacting isolated narrow bands, Proceedings of the National Academy of Sciences **120**, e2217816120 (2023).

[34] D. Mao, J. F. Mendez-Valderrama, and D. Chowdhury, Is the low-energy optical absorption in correlated insulators controlled by quantum geometry?, arXiv preprint arXiv:2410.16352 (2024).

[35] T. M. Wolf, Y.-C. Chao, A. H. MacDonald, and J. J. Su, Intraband collective excitations in fractional chern insulators are dark, arXiv preprint arXiv:2406.10709 (2024).

[36] P. Sharma, Y. Peng, and D. N. Sheng, Topological quantum phase transitions driven by a displacement field in twisted MoTe₂ bilayers, Phys. Rev. B **110**, 125142 (2024).

[37] T. Zaklama, D. Luo, and L. Fu, Structure factor and topological bound of twisted bilayer semiconductors at fractional fillings, arXiv preprint arXiv:2411.03496 (2024).

[38] F. D. M. Haldane, Geometrical Description of the Frac-

tional Quantum Hall Effect, Physical Review Letters **107**, 116801 (2011), publisher: American Physical Society.

[39] S.-F. Liou, F. Haldane, K. Yang, and E. Rezayi, Chiral Gravitons in Fractional Quantum Hall Liquids, Physical Review Letters **123**, 146801 (2019), publisher: American Physical Society.

[40] K. Yang, Acoustic wave absorption as a probe of dynamical geometrical response of fractional quantum hall liquids, Physical Review B **93**, 161302 (2016).

[41] J. Liang, Z. Liu, Z. Yang, Y. Huang, U. Wurstbauer, C. R. Dean, K. W. West, L. N. Pfeiffer, L. Du, and A. Pinczuk, Evidence for chiral graviton modes in fractional quantum hall liquids, Nature **628**, 78 (2024).

[42] Y. Wang, J. Huxford, D. X. Nguyen, G. Ji, Y. B. Kim, and B. Yang, Dynamics and lifetime of geometric excitations in moir\'e systems, arXiv preprint arXiv:2502.02640 (2025).

[43] M. Long, H. Lu, H.-Q. Wu, and Z. Y. Meng, Spectra of magnetoroton and chiral graviton modes of fractional chern insulator, arXiv preprint arXiv:2501.00247 (2024).

[44] A. P. Reddy, N. Paul, A. Abouelkomsan, and L. Fu, Non-Abelian Fractionalization in Topological Minibands, Phys. Rev. Lett. **133**, 166503 (2024).

[45] C. Xu, N. Mao, T. Zeng, and Y. Zhang, Multiple chern bands in twisted mote$_2$ and possible non-abelian states, Phys. Rev. Lett. **134**, 066601 (2025).

[46] C.-E. Ahn, W. Lee, K. Yananose, Y. Kim, and G. Y. Cho, Non-Abelian fractional quantum anomalous Hall states and first Landau level physics of the second moir\'e band of twisted bilayer MoTe$_2$, Phys. Rev. B **110**, L161109 (2024).

[47] C. Wang, X.-W. Zhang, X. Liu, J. Wang, T. Cao, and D. Xiao, Higher landau-level analogs and signatures of non-abelian states in twisted bilayer mote$_2$, Phys. Rev. Lett. **134**, 076503 (2025).

[48] A. Abouelkomsan and L. Fu, Non-Abelian spin Hall insulator, arXiv 10.48550/arXiv.2406.14617 (2024), 2406.14617.

[49] H. Goldman, A. P. Reddy, N. Paul, and L. Fu, Zero-field composite fermi liquid in twisted semiconductor bilayers, Physical Review Letters **131**, 136501 (2023).

[50] J. Dong, J. Wang, P. J. Ledwith, A. Vishwanath, and D. E. Parker, Composite fermi liquid at zero magnetic field in twisted mote 2, Physical Review Letters **131**, 136502 (2023).

[51] A. Abouelkomsan, N. Paul, A. Stern, and L. Fu, Compressible quantum matter with vanishing drude weight, arXiv preprint arXiv:2403.14747 (2024).

[52] A. Stern and L. Fu, Transport properties of a half-filled chern band at the electron and composite fermion phases (2024).

[53] X.-Y. Song, C.-M. Jian, L. Fu, and C. Xu, Intertwined fractional quantum anomalous hall states and charge density waves, Physical Review B **109**, 115116 (2024).

[54] F. Haldane, Many-particle translational symmetries of two-dimensional electrons at rational landau-level filling, Physical review letters **55**, 2095 (1985).

[55] J. Wang, J. Cano, A. J. Millis, Z. Liu, and B. Yang, Exact landau level description of geometry and interaction in a flatband, Physical review letters **127**, 246403 (2021).

[56] B. A. Bernevig and N. Regnault, Emergent many-body translational symmetries of abelian and non-abelian fractionally filled topological insulators, Physical Review B **85**, 075128 (2012).

[57] R. Resta, Drude weight and superconducting weight, J. Phys.: Condens. Matter **30**, 414001 (2018).

[58] A. P. Reddy, F. Alsallom, Y. Zhang, T. Devakul, and L. Fu, Fractional quantum anomalous hall states in twisted bilayer mote$_2$ and wse$_2$, Phys. Rev. B **108**, 085117 (2023).

[59] E. R. Gagliano and C. A. Balseiro, Dynamical Properties of Quantum Many-Body Systems at Zero Temperature, Physical Review Letters **59**, 2999 (1987), publisher: American Physical Society.

Supplemental Material:
Shining light on collective modes in moiré fractional Chern insulators

In this Supplemental Material, we discuss details of roton folding in finite-size periodic systems, the variational ansatz applied to periodically modulated LLs, low-frequency optical absorption in ordinary and periodically modulated LLs, and optical conductivity in periodically modulated LLs and twisted TMDs.

Roton folding in periodic systems and finite-size effects

In this section, we discuss the folding of the roton spectrum in crystalline systems and point out a finite-size effect for the counting of expected folded roton modes based on symmetry considerations. We consider the Hamiltonian of the LLL which takes the form,

$$H = \frac{1}{2} \sum_{\boldsymbol{q}} U(\boldsymbol{q}) : \bar{\rho}_{\boldsymbol{q}}^{\dagger} \bar{\rho}_{\boldsymbol{q}} : \tag{S1}$$

where $\bar{\rho}_{\boldsymbol{q}} = \sum_j e^{-|\boldsymbol{q}|^2 \ell_B^2/4} e^{-i\boldsymbol{q} \cdot \boldsymbol{R}_j}$ is the LL-projected density operator in the $n = 0$ LL in terms of particle guiding center coordinates $\boldsymbol{R}_j$. The interaction $U(\boldsymbol{q})$ is taken to be bare Coulomb $U(\boldsymbol{q}) = \frac{U_0 a_0}{2A} \frac{2\pi}{|\boldsymbol{q}|}$. with the interaction strength $U_0 = e^2/(4\pi\epsilon a_0)$.

As shown by Haldane [54], many-body magnetic translations in this case are factorized into a relative and a center of mass (COM) part. The momentum eigenvalues corresponding to the relative motion can be used to label any many-body state. On a finite torus spanned by two vectors $\boldsymbol{L}_1$ and $\boldsymbol{L}_2$ such that $|\boldsymbol{L}_1 \times \boldsymbol{L}_2| = 2\pi\ell_B^2 N_\phi$, the relative momentum takes discrete values,

$$\boldsymbol{q} \in \text{BZ}_{\text{cont}} = m\boldsymbol{g}_1 + n\boldsymbol{g}_2 \ , \ (m,n) = (0 \ldots N-1, 0 \ldots N-1) \tag{S2}$$

where $N = \text{GCD}(N_p, N_\phi)$ with GCD denoting greatest common divisor, N_p and N_ϕ are the number of particles and flux quanta respectively. $\boldsymbol{g}_1$ and $\boldsymbol{g}_2$ are two reciprocal lattice vectors such that $\boldsymbol{L}_i \cdot \boldsymbol{g}_j = 2\pi\delta_{ij}$. The discretization defines a *many-body* Brillouin zone which we will refer to as BZ_{cont}. As system size increases (while keeping a fixed filling ν), the mesh defined by $\boldsymbol{q}$ becomes denser and larger and in the thermodynamic limit, $\boldsymbol{q} \in R^2$ as expected from a continuous system. In addition to the relative motion, COM motion gives rise to q-fold degeneracy for $\nu = p/q$ such any state at momentum $\boldsymbol{q} = (q_1, q_2)$ is degenerate with other states at $\boldsymbol{q} = (q_1, q_2 + mN)$ for $m = 1, \cdots q-1$.

In Fig S1(a), we show the many-body spectrum obtained from diagonalizing equation (S1) utilizing the many-body quantum numbers $|\boldsymbol{q}|$ at $\nu = 1/3$ (equivalently $\nu = 2/3$). We use a hexagonal torus with $N_\phi = 27$ and equal aspect ratio. We observe as expected the FQH ground state at $|\boldsymbol{q}| = 0$. In addition, the magneto-roton branch is clearly visible. Notice that the magneto-roton minima on this cluster occurs at the K points, defined as $|K|\ell_B \approx 1.6$.

To make connection with periodic crystalline system with a well-defined unit cell and discrete translation symmetry, it's natural to choose the single particle LLL wavefunctions to be magnetic Bloch basis $\phi_{\boldsymbol{k}}(\boldsymbol{r})$ parametrized by a Bloch momentum $\boldsymbol{k}$ [55] that lives in a Brillouin zone which we will refer to as BZ_{Bloch}. This is obtained by defining a unit cell spanned by two vectors $\boldsymbol{a}_1$, $\boldsymbol{a}_2$ that encloses one flux quantum $|\boldsymbol{a}_1 \times \boldsymbol{a}_2| = 2\pi\ell_B^2$ and applying Bloch's theorem. Again, on a finite torus spanned by two vectors $\boldsymbol{L}_1 = N_1\boldsymbol{a}_1$, $\boldsymbol{L}_2 = N_2\boldsymbol{a}_2$ with $N_1 \times N_2 = N_\phi$, we have

$$\mathbf{k} \in \text{BZ}_{\text{Bloch}} = m\boldsymbol{g}_1 + n\boldsymbol{g}_2 \ , \ (m,n) = (0 \ldots N_1-1, 0 \ldots N_2-1) \tag{S3}$$

where $\boldsymbol{L}_i \cdot \boldsymbol{g}_j = 2\pi\delta_{ij}$. The many-body Hamiltonian diagonalized with these quantum numbers *does not* reveal the full many-body symmetries of the problem. In such a case, the total momenta $\boldsymbol{K}_{\text{CM}} = \sum_i^{N_p} \boldsymbol{k}_i$ is *folded* relative to the relative momenta $\boldsymbol{q} \in \text{BZ}_{\text{cont}}$ as $\boldsymbol{k}_i$ is defined only modulo reciprocal lattice vectors $\boldsymbol{G} = m\boldsymbol{G}_1 + n\boldsymbol{G}_2$ with $\boldsymbol{G}_i \cdot \boldsymbol{a}_j = 2\pi\delta_{ij}$ [20, 56].

To illustrate this, we work again with the same hexagonal torus that corresponds to the many-body spectrum in Fig. S1(a). We diagonalize the Hamiltonian (S1) as a function of the Bloch momentum $|\boldsymbol{K}_{\text{CM}}|$. As shown in Fig
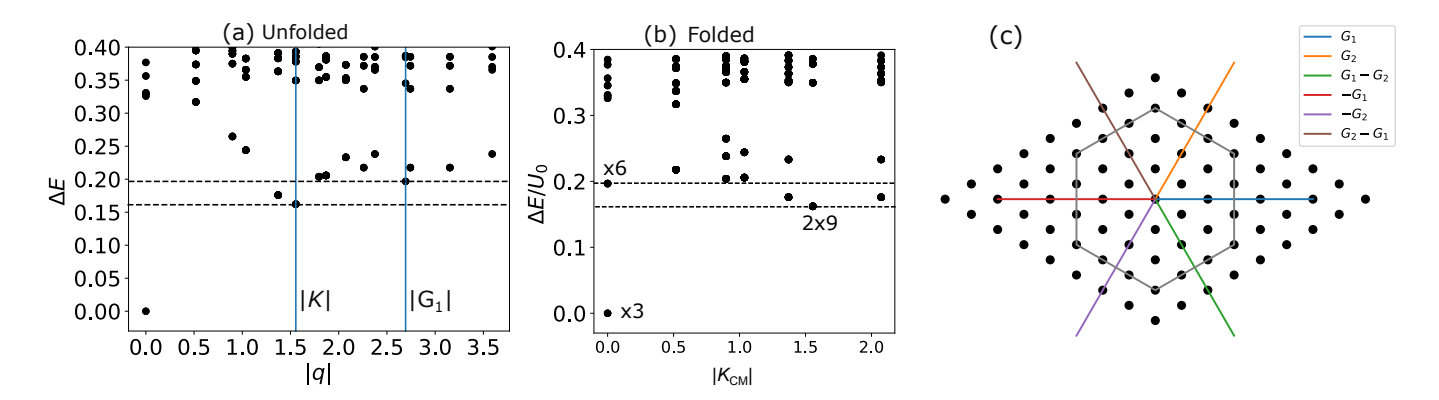
FIG. S1. (a) The unfolded $\nu = 1/3$ many-body spectrum as a function of $|\boldsymbol{q}| \in \mathrm{BZ}_{\mathrm{cont}}$ (equation (S2)) obtained on a hexagonal torus with $N_\phi = 27$ and equal aspect ratio. The vertical lines denote the magnitude of the momentum points $\boldsymbol{K}$ (corner points of $\mathrm{BZ}_{\mathrm{Bloch}}$) and $\boldsymbol{G}_1$ (reciprocal lattice vector of $\mathrm{BZ}_{\mathrm{Bloch}}$) (c.f. panel (c)). (b) The folded $\nu = 1/3$ many-body spectrum on the same finite system plotted as a function of $|\boldsymbol{K}_{\mathrm{CM}}| \in \mathrm{BZ}_{\mathrm{Bloch}}$ (equation (S3)) obtained from working with magnetic Bloch wavefunction for the LLL. (c) Illustration of $\mathrm{BZ}_{\mathrm{cont}}$ (all black points) and $\mathrm{BZ}_{\mathrm{Bloch}}$ (all black points bounded by the hexagon) for a hexagonal torus with $N_1 \times N_2 = N_\phi = 27$. One immediately sees that not all first shell $\boldsymbol{G}$ lie in $\mathrm{BZ}_{\mathrm{cont}}$. Only $\boldsymbol{G}_1$ and $-\boldsymbol{G}_1$ lie in $\mathrm{BZ}_{\mathrm{cont}}$ which means only two states (for each topologically distinct ground state) fold back to $\boldsymbol{K}_{\mathrm{CM}} = 0$ giving rise to total of six states as shown in panel (b).

S1(b), the many-body energy states are folded relative to what is plotted in Fig. S1(a). In addition, the many-body spectrum now contains multiple degeneracies from the COM motion that have been factored out in the spectrum shown Fig. S1(a).

To study the low-lying excitations of crystalline systems which do not exhibit continuous translational symmetry and have momentum only defined modulo $\boldsymbol{G}$, it's crucial to understand the number of states that fold back to a generic many-body Bloch momenta $K_{\mathrm{CM}} \in \mathrm{BZ}_{\mathrm{Bloch}}$ from a momentum point $\boldsymbol{q} \in \mathrm{BZ}_{\mathrm{cont}}$. Since K_{CM} is defined only modulo $\boldsymbol{G}$, all states at momentum $\boldsymbol{q} = K_{\mathrm{CM}} + \boldsymbol{G}$ will map back to K_{CM}.

As we discussed earlier, the momentum $\boldsymbol{q} \in \mathrm{BZ}_{\mathrm{cont}}$ is discretized on a finite torus. While all $\boldsymbol{G}$ are equivalent in a crystalline system with discrete translational symmetry, they are physically distinct momenta in the $\mathrm{BZ}_{\mathrm{cont}}$. *Crucially*, on a finite system, $\mathrm{BZ}_{\mathrm{cont}}$ will not contain all distinct $\boldsymbol{G}$ in it. It's only in thermodyanmic limit that $\mathrm{BZ}_{\mathrm{cont}} \to R^2$ and therefore all $\boldsymbol{G}$ are covered. Also, as a finite size effect, not all $\boldsymbol{G}$ related by rotation can exist in the $\mathrm{BZ}_{\mathrm{cont}}$ in finite system. In our example (Fig. S1(b)), naively one expects (based on the folding picture) a low-lying set of $3 \times 6 = 18$ states at $\boldsymbol{K}_{\mathrm{CM}} \equiv \Gamma = 0$ above the ground state. These are the rotons that fold from the first shell $\boldsymbol{q} = m\boldsymbol{G}_1 + n\boldsymbol{G}_2$ for $(m, n) = (1, 0), (0, 1), (1, -1), (-1, 1), (-1, 0), (0, -1)$ which are related by C_6 rotation. The factor of 3 corresponds to the three topologically degenerate ground states. However, we only observe 6 states at $K_{\mathrm{CM}} = \Gamma$ (Fig. S1(b). To understand the origin of these, we plot in Fig. S1(c) the distinct $\boldsymbol{q} \in \mathrm{BZ}_{\mathrm{cont}}$ and the distinct $K_{\mathrm{CM}} \in \mathrm{BZ}_{\mathrm{Bloch}}$ for the finite system we work with. We observe that $\mathrm{BZ}_{\mathrm{FQH}}$ can only fit two $\boldsymbol{G}$ vectors out of the first shell. This gives rise to two states for each topologically distinct ground state leading to total of six states which what we observe in Fig. S1(b) at $K_{\mathrm{CM}} = \Gamma$.

Unfortunately, this finite size effect exist for all numerically accessible finite size systems which poses a challenge in studying the properties of the fractional exciton as we only observe a subset of of the states that fold from the first shell $\boldsymbol{G}$ vectors. On the other hand, the situation is less drastic for the K and K' rotons. Based on the folding picture, we expect three low-lying states for each ground state corresponding to three equivalent K or K' point giving rise to a total of 9 states. Indeed, this is what we observe in Fig. S1(b).

In all cases, on all accessible finite size systems, we cannot access states that fold from momentum points beyond the first shell of $\boldsymbol{G}$ vectors. However, these states will be generally higher in energy and most likely won't contribute to the low energy properties of the system.

Variational ansatz in periodically modulated Landau levels

In this section, we detail the application of the variational ansatz to the periodically modulated lowest Landau level (LLL). We study the LLL perturbed by a weak periodic potential enclosing one flux quantum per unit cell. We recall

the projected Hamiltonian

$$H = \sum_{\boldsymbol{G}} V_{\boldsymbol{G}} \bar{\rho}_{\boldsymbol{G}} + \frac{1}{2} \sum_{\boldsymbol{q}} U(\boldsymbol{q}) \bar{\rho}_{\boldsymbol{q}}^{\dagger} \bar{\rho}_{\boldsymbol{q}} \tag{S4}$$

where $\bar{\rho}_{\boldsymbol{q}} = \sum_j e^{-|\boldsymbol{q}|^2 \ell_B^2/4} e^{-i\boldsymbol{q}\cdot\boldsymbol{R}_j}$ is the LL-projected density operator in terms of particle guiding center coordinates $\boldsymbol{R}_j$, and we've dropped the normal ordering for convenience. It is helpful to distinguish two levels of approximation: (1) the variational approximation and (2) the variational *and* perturbative ($V_{\boldsymbol{G}} \ll$ Coulomb) approximation. Both approximations are in the band-projected limit where the cyclotron gap $\hbar\omega_c$ is the largest energy scale.

(1) Variational.— Recall that our variational ansatz is

$$|\phi_{\boldsymbol{q}}^{\alpha}\rangle = \sum_{\boldsymbol{G}} c_{\boldsymbol{q}+\boldsymbol{G}}^{\alpha} \bar{\rho}_{\boldsymbol{q}+\boldsymbol{G}} |0\rangle \tag{S5}$$

where $\boldsymbol{q} \in$ BZ and $\boldsymbol{G}$ is a reciprocal lattice vector, which has energy

$$E_{\boldsymbol{q}}^{\alpha} - E_0 = \frac{\sum_{\boldsymbol{G}_1 \boldsymbol{G}_2} c_{\boldsymbol{q}+\boldsymbol{G}_1}^{\alpha*} c_{\boldsymbol{q}+\boldsymbol{G}_2}^{\alpha} \langle 0|\bar{\rho}_{\boldsymbol{q}+\boldsymbol{G}_1}^{\dagger}[H, \bar{\rho}_{\boldsymbol{q}+\boldsymbol{G}_2}]|0\rangle}{\sum_{\boldsymbol{G}_1 \boldsymbol{G}_2} c_{\boldsymbol{q}+\boldsymbol{G}_1}^{\alpha*} c_{\boldsymbol{q}+\boldsymbol{G}_2}^{\alpha} \bar{s}(\boldsymbol{q}, \boldsymbol{G}_1, \boldsymbol{G}_2)} \tag{S6}$$

where $(H - E_0)|0\rangle = 0$ and $\bar{s}(\boldsymbol{q}, \boldsymbol{G}_1, \boldsymbol{G}_2) = \langle 0|\bar{\rho}_{\boldsymbol{q}+\boldsymbol{G}_1}^{\dagger} \bar{\rho}_{\boldsymbol{q}+\boldsymbol{G}_2}|0\rangle$ is the projected static structure factor. If we also assume that $c_{\boldsymbol{q}+\boldsymbol{G}}^{\alpha*} = c_{-\boldsymbol{q}-\boldsymbol{G}}^{\alpha}$, a constraint on our ansatz which is natural in the presence of parity symmetry, then the above can be written as

$$E_{\boldsymbol{q}}^{\alpha} - E_0 = \frac{1}{2} \frac{\sum_{\boldsymbol{G}_1 \boldsymbol{G}_2} c_{\boldsymbol{q}+\boldsymbol{G}_1}^{\alpha*} c_{\boldsymbol{q}+\boldsymbol{G}_2}^{\alpha} \langle 0|[\bar{\rho}_{\boldsymbol{q}+\boldsymbol{G}_1}^{\dagger}, [H, \bar{\rho}_{\boldsymbol{q}+\boldsymbol{G}_2}]]|0\rangle}{\sum_{\boldsymbol{G}_1 \boldsymbol{G}_2} c_{\boldsymbol{q}+\boldsymbol{G}_1}^{\alpha*} c_{\boldsymbol{q}+\boldsymbol{G}_2}^{\alpha} \bar{s}(\boldsymbol{q}, \boldsymbol{G}_1, \boldsymbol{G}_2)}. \tag{S7}$$

Using the Girvin-Macdonald-Platzman algebra [19]

$$[\bar{\rho}_{\boldsymbol{q}_1}, \bar{\rho}_{\boldsymbol{q}_2}] = f_{\boldsymbol{q}_1}^{\boldsymbol{q}_2} \bar{\rho}_{\boldsymbol{q}_1+\boldsymbol{q}_2}, \qquad f_{\boldsymbol{q}_1}^{\boldsymbol{q}_2} = 2i e^{\boldsymbol{q}_1 \cdot \boldsymbol{q}_2 \ell_B^2/2} \sin(\boldsymbol{q}_1 \wedge \boldsymbol{q}_2 \ell_B^2/2), \tag{S8}$$

we can simplify the variational energies. It is useful to collect the following expressions:

$$[H, \bar{\rho}_{\boldsymbol{q}+\boldsymbol{G}_2}] = \sum_{\boldsymbol{G}} V_{\boldsymbol{G}} f_{\boldsymbol{G}}^{\boldsymbol{q}+\boldsymbol{G}_2} \bar{\rho}_{\boldsymbol{q}+\boldsymbol{G}+\boldsymbol{G}_2} + \frac{1}{2} \sum_{\boldsymbol{q}'} U(\boldsymbol{q}') f_{\boldsymbol{q}'}^{\boldsymbol{q}+\boldsymbol{G}_2} \{\bar{\rho}_{\boldsymbol{q}+\boldsymbol{q}'+\boldsymbol{G}_2}, \bar{\rho}_{-\boldsymbol{q}'}\}$$

$$\frac{1}{2}[\bar{\rho}_{-\boldsymbol{q}-\boldsymbol{G}_1}, [H, \bar{\rho}_{\boldsymbol{q}+\boldsymbol{G}_2}]] =$$
$$\frac{1}{2} \sum_{\boldsymbol{G}} V_{\boldsymbol{G}} f_{\boldsymbol{G}}^{\boldsymbol{q}+\boldsymbol{G}_2} f_{-\boldsymbol{q}-\boldsymbol{G}_1}^{\boldsymbol{q}+\boldsymbol{G}+\boldsymbol{G}_2} \bar{\rho}_{-\boldsymbol{G}_1+\boldsymbol{G}+\boldsymbol{G}_2} + \frac{1}{4} \sum_{\boldsymbol{q}'} U(\boldsymbol{q}') f_{\boldsymbol{q}'}^{\boldsymbol{q}+\boldsymbol{G}_2} \left(f_{-\boldsymbol{q}-\boldsymbol{G}_1}^{-\boldsymbol{q}'} \{\bar{\rho}_{-\boldsymbol{q}-\boldsymbol{q}'-\boldsymbol{G}_1}, \bar{\rho}_{\boldsymbol{q}+\boldsymbol{q}'+\boldsymbol{G}_2}\} + f_{-\boldsymbol{q}-\boldsymbol{G}_1}^{\boldsymbol{q}+\boldsymbol{q}'+\boldsymbol{G}_2} \{\bar{\rho}_{\boldsymbol{q}'+\boldsymbol{G}_2-\boldsymbol{G}_1}, \bar{\rho}_{-\boldsymbol{q}'}\} \right)$$
$$\tag{S9}$$

where we've assumed the interaction satisfies $U(\boldsymbol{q}) = U(-\boldsymbol{q}')$ and $\{A, B\} = AB + BA$. Altogether, the energy without assuming parity symmetry (Eq. (S6)) becomes

$$E_{\boldsymbol{q}}^{\alpha} - E_0 = \frac{\sum_{\boldsymbol{G}_1 \boldsymbol{G}_2} c_{\boldsymbol{q}+\boldsymbol{G}_1}^{\alpha*} c_{\boldsymbol{q}+\boldsymbol{G}_2}^{\alpha} \left(\sum_{\boldsymbol{G}} V_{\boldsymbol{G}} f_{\boldsymbol{G}}^{\boldsymbol{q}+\boldsymbol{G}_2} \bar{s}(\boldsymbol{q}, \boldsymbol{G}_1, \boldsymbol{G}+\boldsymbol{G}_2) + \frac{1}{2} \sum_{\boldsymbol{q}'} U(\boldsymbol{q}') f_{\boldsymbol{q}'}^{\boldsymbol{q}+\boldsymbol{G}_2} \langle 0|\bar{\rho}_{-\boldsymbol{q}-\boldsymbol{G}_1} \{\bar{\rho}_{\boldsymbol{q}+\boldsymbol{q}'+\boldsymbol{G}_2}, \bar{\rho}_{-\boldsymbol{q}'}\}|0\rangle \right)}{\sum_{\boldsymbol{G}_1 \boldsymbol{G}_2} c_{\boldsymbol{q}+\boldsymbol{G}_1}^{\alpha*} c_{\boldsymbol{q}+\boldsymbol{G}_2}^{\alpha} \bar{s}(\boldsymbol{q}, \boldsymbol{G}_1, \boldsymbol{G}_2)}$$
$$\tag{S10}$$

and the energy assuming parity (Eq. (S7)) becomes

$$E_{\boldsymbol{q}}^{\alpha} - E_0 = \frac{\sum_{\boldsymbol{G}_1 \boldsymbol{G}_2} c_{\boldsymbol{q}+\boldsymbol{G}_1}^{\alpha*} c_{\boldsymbol{q}+\boldsymbol{G}_2}^{\alpha} \left(\frac{1}{2} \sum_{\boldsymbol{G}} V_{\boldsymbol{G}} f_{\boldsymbol{G}}^{\boldsymbol{q}+\boldsymbol{G}_2} f_{-\boldsymbol{q}-\boldsymbol{G}_1}^{\boldsymbol{q}+\boldsymbol{G}+\boldsymbol{G}_2} \langle 0|\bar{\rho}_{-\boldsymbol{G}_1+\boldsymbol{G}_2+\boldsymbol{G}}|0\rangle + \frac{1}{4} \sum_{\boldsymbol{q}'} U(\boldsymbol{q}') f_{\boldsymbol{q}'}^{\boldsymbol{q}+\boldsymbol{G}_2} T_{\boldsymbol{G}_1, \boldsymbol{G}_2}^{\boldsymbol{q}, \boldsymbol{q}'} \right)}{\sum_{\boldsymbol{G}_1 \boldsymbol{G}_2} c_{\boldsymbol{q}+\boldsymbol{G}_1}^{\alpha*} c_{\boldsymbol{q}+\boldsymbol{G}_2}^{\alpha} \bar{s}(\boldsymbol{q}, \boldsymbol{G}_1, \boldsymbol{G}_2)} \tag{S11}$$

where

$$T_{\boldsymbol{G}_1, \boldsymbol{G}_2}^{\boldsymbol{q}, \boldsymbol{q}'} = f_{-\boldsymbol{q}-\boldsymbol{G}_1}^{-\boldsymbol{q}'} (\bar{s}(\boldsymbol{q}+\boldsymbol{q}', \boldsymbol{G}_1, \boldsymbol{G}_2) + \bar{s}(-\boldsymbol{q}-\boldsymbol{q}', -\boldsymbol{G}_2, -\boldsymbol{G}_1)) + f_{-\boldsymbol{q}-\boldsymbol{G}_1}^{\boldsymbol{q}+\boldsymbol{q}'+\boldsymbol{G}_2} (\bar{s}(-\boldsymbol{q}', \boldsymbol{G}_{12}, 0) + \bar{s}(\boldsymbol{q}', 0, \boldsymbol{G}_{21})). \tag{S12}$$

We remark that Eq. (S10) involves the structure factor and a three-density expectation value, while Eq. (S11) only involves the structure factor and single-density expectation value. Naturally, the latter is easier to compute, but either may be computed numerically in principle for finite-size systems.

(2) *Variational + perturbative.*— The perturbative variational calculation assumes V is small, where

$$H = H_C + V, \quad H_C = \frac{1}{2}\sum_{\boldsymbol{q}} U(\boldsymbol{q})\bar{\rho}_{\boldsymbol{q}}^{\dagger}\bar{\rho}_{\boldsymbol{q}}, \quad V = \sum_{\boldsymbol{G}} V_{\boldsymbol{G}}\bar{\rho}_{\boldsymbol{G}}. \tag{S13}$$

Let us denote the eigenstates and energies of the Coulomb Hamiltonian $\hat{H}_C$ by $|\Psi_{\boldsymbol{k},m}^{(0)}\rangle$ and $E_{\boldsymbol{k},m}^{(0)}$, where $\boldsymbol{k}$ denotes (unrestricted) many-body momentum and m distinguishes states with the same $\boldsymbol{k}$. We assume that the Coulomb ground state is a translationally invariant liquid (valid for FQH states) and denote it $|\Psi_0^{(0)}\rangle$. We also label the unperturbed energies in the crystal Brillouin zone as band energies by $E_{\boldsymbol{k},m}^{(0)}$, with the (unperturbed) ground state energy denoted by $E_0^{(0)}$. We consider states of the form

$$|\phi_{\boldsymbol{k}}^{(0)}\rangle = \frac{1}{\sqrt{\bar{s}_0(\boldsymbol{k})}}\bar{\rho}_{\boldsymbol{k}}|\Psi_0^{(0)}\rangle \tag{S14}$$

where $\bar{s}_0(\boldsymbol{k}) = \langle\Psi_0^{(0)}|\bar{\rho}_{-\boldsymbol{k}}\bar{\rho}_{\boldsymbol{k}}|\Psi_0^{(0)}\rangle$. In the variational + perturbative approach, for any $\boldsymbol{k}$, we diagonalize H in the subspace spanned by the $|\phi_{\boldsymbol{k}+\boldsymbol{G}}^{(0)}\rangle$ to leading order in V. We give two examples for high-symmetry points below.

Fractional exciton.— We project V into the manifold of 6 SMA states which are connected via V to Γ:

$$\begin{aligned}
\langle\phi_{\boldsymbol{G}_i}^{(0)}|\hat{V}|\phi_{\boldsymbol{G}_j}^{(0)}\rangle &= V_{\boldsymbol{G}_i-\boldsymbol{G}_j}\langle\phi_{\boldsymbol{G}_i}^{(0)}|\bar{\rho}_{\boldsymbol{G}_i-\boldsymbol{G}_j}|\phi_{\boldsymbol{G}_j}^{(0)}\rangle \\
&= \frac{V_{\boldsymbol{G}_i-\boldsymbol{G}_j}}{N\bar{s}_0(\boldsymbol{G})}\langle 0|\bar{\rho}_{-\boldsymbol{G}_i}\bar{\rho}_{\boldsymbol{G}_i-\boldsymbol{G}_j}\bar{\rho}_{\boldsymbol{G}_j}|0\rangle
\end{aligned} \tag{S15}$$

where we denote $\bar{s}_0(\boldsymbol{G}_i)$, which are equal for all i, by $\bar{s}_0(\boldsymbol{G})$. We assume

$$V_{\boldsymbol{G}_1} = V_{\boldsymbol{G}_3} = V_{\boldsymbol{G}_5} = V_{\boldsymbol{G}_2}^* = V_{\boldsymbol{G}_4}^* = V_{\boldsymbol{G}_6}^* = -V_0 \tag{S16}$$

and we define

$$S_3 = \langle 0|\bar{\rho}_{\boldsymbol{G}_1}\bar{\rho}_{\boldsymbol{G}_3}\bar{\rho}_{\boldsymbol{G}_5}|0\rangle. \tag{S17}$$

Then the Hamiltonian in this subspace can be written

$$H|_{\Gamma} = \Delta_{\boldsymbol{G}} - \frac{1}{\bar{s}_0(\boldsymbol{G})}\begin{pmatrix}
0 & V_0^*S_3 & 0 & 0 & 0 & V_0^*S_3^* \\
V_0 S_3^* & 0 & V_0 S_3 & 0 & 0 & 0 \\
0 & V_0^*S_3^* & 0 & V_0^*S_3 & 0 & 0 \\
0 & 0 & V_0 S_3^* & 0 & V_0 S_3 & 0 \\
0 & 0 & 0 & V_0^*S_3^* & 0 & V_0^*S_3 \\
V_0 S_3 & 0 & 0 & 0 & V_0 S_3^* & 0
\end{pmatrix} \tag{S18}$$

where $\Delta_{\boldsymbol{G}} = \langle\Psi_{\boldsymbol{G}_i,0}^{(0)}|H_C - E_0^{(0)}|\Psi_{\boldsymbol{G}_i,0}^{(0)}\rangle$ (for all i) is the exact Coulomb energy of the lowest excitation at $\boldsymbol{G}_i$. We introduce C_3-angular momentum eigenstates parity-related

$$\begin{aligned}
|\ell,1\rangle &= \frac{1}{\sqrt{3}}(|\phi_{\boldsymbol{G}_1}^{(0)}\rangle + e^{2\pi i\ell/3}|\phi_{\boldsymbol{G}_3}^{(0)}\rangle + e^{4\pi i\ell/3}|\phi_{\boldsymbol{G}_5}^{(0)}\rangle) \\
|\ell,2\rangle &= \frac{1}{\sqrt{3}}(|\phi_{\boldsymbol{G}_2}^{(0)}\rangle + e^{2\pi i\ell/3}|\phi_{\boldsymbol{G}_4}^{(0)}\rangle + e^{4\pi i\ell/3}|\phi_{\boldsymbol{G}_6}^{(0)}\rangle)
\end{aligned} \tag{S19}$$

for $\ell = -1, 0, 1$. The lowest fractional exciton is a linear combination of the above states with angular momentum $\ell = \arg\max_{\ell}[\cos(\psi + \ell\pi/3)]$ and energy

$$E_0^{(1)} = E_0^{(0)} + \Delta_{\boldsymbol{G}} - 2\frac{|V_0\eta|}{\bar{s}_0(\boldsymbol{G})}\max_{\ell}[\cos(\psi + \ell\pi/3)], \tag{S20}$$

where $S_3 = |S_3|e^{i\psi}$ (the phase of V_0 does not enter).

K-*roton.*— The points K_1, K_2, K_3 satisfy $K_1 - K_2 = \boldsymbol{G}_2, K_2 - K_3 = \boldsymbol{G}_4, K_3 - K_1 = \boldsymbol{G}_6$. The Hamiltonian in this subspace is

$$
\begin{aligned}
H\mid_K &= \Delta_K + \frac{1}{\bar{s}_0(K)}
\begin{pmatrix}
0 & V_{K_1-K_2}\langle 0|\bar{\rho}_{-K_1}\bar{\rho}_{K_1-K_2}\bar{\rho}_{K_2}|0\rangle & V_{K_1-K_3}\langle 0|\bar{\rho}_{-K_1}\bar{\rho}_{K_1-K_3}\bar{\rho}_{K_3}|0\rangle \\
V_{K_2-K_1}\langle 0|\bar{\rho}_{-K_2}\bar{\rho}_{K_2-K_1}\bar{\rho}_{K_1}|0\rangle & 0 & V_{K_2-K_3}\langle 0|\bar{\rho}_{-K_2}\bar{\rho}_{K_2-K_3}\bar{\rho}_{K_3}|0\rangle \\
V_{K_3-K_1}\langle 0|\bar{\rho}_{-K_3}\bar{\rho}_{K_3-K_1}\bar{\rho}_{K_1}|0\rangle & V_{K_3-K_2}\langle 0|\bar{\rho}_{-K_3}\bar{\rho}_{K_3-K_2}\bar{\rho}_{K_2}|0\rangle & 0
\end{pmatrix} \\
&= \Delta_K - \frac{1}{\bar{s}_0(K)}
\begin{pmatrix}
0 & V_0^* S_3 & V_0 S_3^* \\
V_0 S_3^* & 0 & V_0^* S_3 \\
V_0^* S_3 & V_0 S_3^* & 0
\end{pmatrix}
\end{aligned}
\tag{S21}
$$

where we defined $\bar{s}_0(K) \equiv \bar{s}_0(K_i)$ (for $i = 1, 2, 3$) and now

$$
S_3 = \langle 0|\bar{\rho}_{-K_1}\bar{\rho}_{K_2-K_1}\bar{\rho}_{K_2}|0\rangle
\tag{S22}
$$

(not to be confused with Eq. (S17)). We introduce the C_3-angular momentum eigenstate

$$
|\ell\rangle = \frac{1}{\sqrt{3}} \sum_{j=0}^{2} e^{2\pi i j\ell/3} |\phi_{K_j}^{(0)}\rangle.
\tag{S23}
$$

The lowest K-roton is the angular momentum eigenstate with $\ell = \arg\max_\ell[\cos(\psi + 2\pi\ell/3)]$ and energy

$$
E_K^{(0)} = E_0^{(0)} + \Delta_K - 2\frac{|V_0 S_3|}{\bar{s}_0(K)} \max_\ell[\cos(\psi + 2\pi\ell/3)]
\tag{S24}
$$

where $\Delta_K = \langle \Psi_{K,0}^{(0)}|H_C - E_0^{(0)}|\Psi_{K,0}^{(0)}\rangle$ and $V_0 S_3 = |V_0 S_3|e^{i\psi}$. Note that unlike the case for the fractional exciton, the phase of V_0 enters $E_K^{(0)}$.

Low-energy spectral weight in ordinary Landau levels

It is a well-known corollary of Kohn's theorem that the low-energy optical spectral weight of an ordinary Landau level system vanishes. For completeness, we review a derivation here, originally due to GMP [19]. We have

$$
\begin{aligned}
W &= \frac{\pi e^2}{2\hbar^2 A} \lim_{q\to 0} \frac{1}{q^2} \langle 0|[\bar{\rho}_{\boldsymbol{q}}^\dagger, [\bar{H}, \bar{\rho}_{\boldsymbol{q}}]]|0\rangle \\
&\equiv \frac{\pi e^2}{\hbar^2 A} \lim_{q\to 0} \frac{1}{q^2} F(\boldsymbol{q}).
\end{aligned}
\tag{S25}
$$

In an ordinary Landau level, the projected Hamiltonian has only the interaction piece, $\bar{H} = \frac{1}{2}\sum_{\boldsymbol{q}'} U(\boldsymbol{q}')\bar{\rho}_{\boldsymbol{q}'}^\dagger\bar{\rho}_{\boldsymbol{q}'}$. Then $F(\boldsymbol{q})$ may be evaluated using the GMP algebra Eq. (S8). We quote the result from Eq. (S9) (we use $\bar{s}(\boldsymbol{q}) = \bar{s}(-\boldsymbol{q})$ in the parity-symmetric Landau level):

$$
\begin{aligned}
F(\boldsymbol{q}) &= \frac{1}{4}\sum_{\boldsymbol{q}'} U(\boldsymbol{q}') f_{\boldsymbol{q}'}^{\boldsymbol{q}} \left(f_{-\boldsymbol{q}}^{-\boldsymbol{q}'} \langle 0|\{\bar{\rho}_{-\boldsymbol{q}-\boldsymbol{q}'}, \bar{\rho}_{\boldsymbol{q}+\boldsymbol{q}'}\}|0\rangle + f_{-\boldsymbol{q}}^{\boldsymbol{q}+\boldsymbol{q}'} \langle 0|\{\bar{\rho}_{\boldsymbol{q}'}, \bar{\rho}_{-\boldsymbol{q}'}\}|0\rangle \right) \\
&= \frac{1}{2}\sum_{\boldsymbol{q}'} U(\boldsymbol{q}') f_{\boldsymbol{q}'}^{\boldsymbol{q}} \left(f_{\boldsymbol{q}}^{\boldsymbol{q}'} \bar{s}(\boldsymbol{q}+\boldsymbol{q}') + f_{-\boldsymbol{q}}^{\boldsymbol{q}+\boldsymbol{q}'} \bar{s}(\boldsymbol{q}') \right)
\end{aligned}
\tag{S26}
$$

where $f_{\boldsymbol{q}}^{\boldsymbol{q}'} = 2ie^{\boldsymbol{q}\cdot\boldsymbol{q}'\ell_B^2/2}\sin(\boldsymbol{q}\wedge\boldsymbol{q}'\ell_B^2/2)$ and $\bar{s}(\boldsymbol{q})$ is the projected structure factor. We expand at small $\boldsymbol{q}$ to obtain

$$
F(\boldsymbol{q}) = \frac{1}{2}(2i)^2 \sum_{\boldsymbol{q}'} U(\boldsymbol{q}')(\boldsymbol{q}'\wedge\boldsymbol{q}\ell_B^2/2)^2 (\bar{s}(\boldsymbol{q}+\boldsymbol{q}') - \bar{s}(\boldsymbol{q}')) + \cdots
\tag{S27}
$$

where subleading terms are higher order in $|q|$. Next, using parity symmetry, it is possible to show that the leading term above vanishes, and hence that $F(\boldsymbol{q})$ vanishes to at least order q^4. It follows that W vanishes identically.

Low-energy spectral weight for modulated Landau levels

In this section, we derive the formula for the low-energy sum rule for modulated Landau levels (Eq. (17) in the main text) using another approach based on projected current operators that gives the same final answer. It is first instructive to review the general formalism for projected observables before applying it to a Chern band (or Landau level).

Projection: general formalism.— Assume our Hamiltonian can be written as

$$H = T + V, \qquad T = \sum_n \varepsilon_n P_n \tag{S28}$$

where ε_n are unperturbed energies, P_n is a projection onto the n'th energy eigenspace, and $|V| \ll |\varepsilon_n - \varepsilon_m|$ for all n, m. Then one may wish to consider the projected Hamiltonian and projected observables in the n'th eigenspace.

Let's focus on the projected Hamiltonian first. Throughout we use the overbar to denote operators defined only on the projected Hilbert space. We wish to find an operator $\bar{H}_n$ such that if $H|\psi_i\rangle = E_i|\psi_i\rangle$ is a solution to the full Schrödinger equation, where $E_i = \varepsilon_n + O(V)$, then $\bar{H}_n|\bar{\psi}_i\rangle = E_i|\bar{\psi}_i\rangle$, where $|\bar{\psi}_i\rangle = P_n|\psi_i\rangle$. The solution to leading order is

$$\bar{H}_n = \varepsilon_n + P_n V P_n + \sum_{m \neq n} \frac{1}{\varepsilon_n - \varepsilon_m} P_n V P_m V P_n + \mathcal{O}(V^3). \tag{S29}$$

Next, given some operator M and two not necessarily distinct eigenvectors of H denoted $|\psi_1\rangle$, $|\psi_2\rangle$ in the *same* manifold of states near E_n, we want to find the operator $\bar{M}$, defined only on the projected Hilbert space, such that

$$\langle \psi_1 | M | \psi_2 \rangle = \langle \bar{\psi}_1 | \bar{M} | \bar{\psi}_2 \rangle, \qquad |\bar{\psi}_i\rangle = P_n |\psi_i\rangle. \tag{S30}$$

The solution to leading order is

$$\bar{M} = P_n M P_n + \sum_{m \neq n} \frac{P_n M P_m V P_n - P_n V P_m M P_n}{\varepsilon_n - \varepsilon_m} + \mathcal{O}(V^2). \tag{S31}$$

Finally, given some operator M and two distinct eigenvectors of H denoted $|\psi_1\rangle$, $|\psi_2\rangle$ in *different* manifolds of states near E_n and E_m respectively $(n \neq m)$, we want to find the operator $\tilde{M}$ satisfying

$$\langle \psi_1 | M | \psi_2 \rangle = \langle \bar{\psi}_1 | \bar{M} | \bar{\psi}_2 \rangle, \qquad |\bar{\psi}_1\rangle = P_n |\psi_1\rangle, \quad |\bar{\psi}_2\rangle = P_m |\psi_2\rangle. \tag{S32}$$

The solution is

$$\bar{M} = P_n M P_m + \sum_{\ell \neq m} \frac{P_n M P_\ell V P_m}{\varepsilon_m - \varepsilon_\ell} + \sum_{\ell \neq n} \frac{P_n V P_\ell M P_m}{\varepsilon_n - \varepsilon_\ell} + \mathcal{O}(V^2). \tag{S33}$$

Landau level projected theory.— Quite generally, we consider electrons in a magnetic field and both 1-body and 2-body potentials:

$$H = \sum_i H_0(\boldsymbol{p}_i - e\boldsymbol{A}) + V(\boldsymbol{r}_i) + \frac{1}{2} \sum_{i \neq j} U(\boldsymbol{r}_i - \boldsymbol{r}_j) \tag{S34a}$$

$$= H_0 + H_C \tag{S34b}$$

where $H_0(\boldsymbol{p}) = p^2/2m$ and $\boldsymbol{A}$ describes a uniform magnetic field $B\hat{z}$. If $V = 0$ and U preserve Galilean invariance, then Kohn's theorem implies

$$\sigma_{\alpha\alpha}(\omega) = \frac{\pi e^2 n}{2m} \left(\delta(\omega - \omega_c) + \delta(\omega + \omega_c) \right). \tag{S35}$$

Again, we'll be interested in the low-energy spectral weight for when Galilean invariance is broken and Λ is intermediate between the strengths of V and $\hbar\omega_c$. With Galilean invariance, W vanishes. Turning on V breaks Galilean invariance and W could be nonvanishing.

For $V, U \ll \omega_c$, we can project the current density operator to a Landau level. The current density operator is

$$\boldsymbol{j} = -\frac{e(\boldsymbol{p} + e\boldsymbol{A})}{mA} = \frac{ie\omega_c}{A} \left(a^\dagger \boldsymbol{d}^* - a\boldsymbol{d} \right) \tag{S36}$$

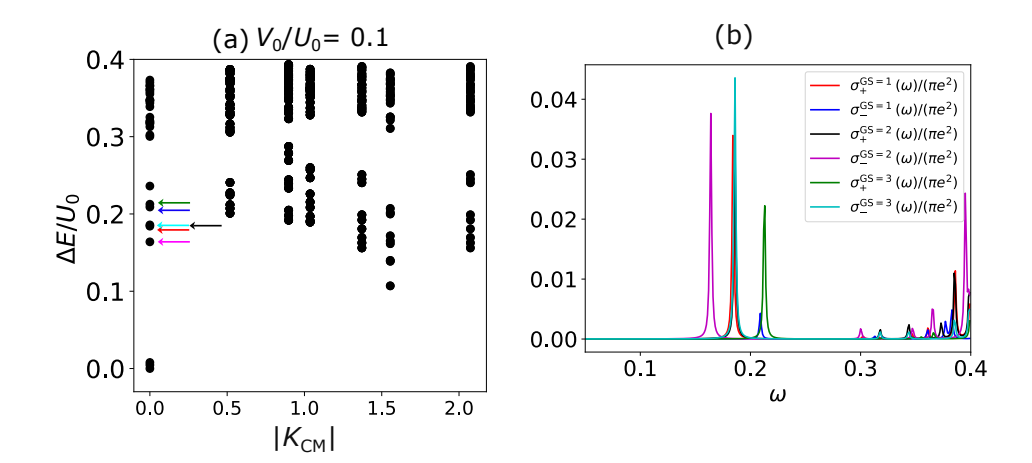FIG. S2. (a) The many-body spectrum at $\nu = 1/3$ for the Hamiltonian (S39) at a function of $|\boldsymbol{K}_{\mathrm{CM}}|$. (b) Left/right circulary polarized optical conductivity $\sigma_{\pm}^{\mathrm{GS}}(\omega)$ calculated the three quasi-degenerate FCI ground states. The peaks position correspond to low-lying fractional exciton states which are highlighted in panel (a). An artificial broadening $\eta = 0.01\,U_0$ is introduced for clarity and $\hbar = 1$. Calculations were done on a 27 site cluster with equal aspect ratio similar to Fig. S1(b). $U_0 = e^2/(4\pi\epsilon a_0)$ is interaction strength.

where $\boldsymbol{A}$ is the gauge field and A is the area. Moreover, $\boldsymbol{d} = (\ell_B, i\ell_B)^T/\sqrt{2}$. Consequently, the projected current density operator is

$$
\begin{aligned}
\bar{\boldsymbol{j}} &= \frac{1}{\hbar\omega_c} P_n \boldsymbol{j} (P_{n-1} - P_{n+1}) H_C P_n + \text{h.c.} \\
&= -\frac{ie}{\hbar A} \left(P_n a^\dagger \boldsymbol{d}^* P_{n-1} H_C P_n + P_n a \boldsymbol{d} P_{n+1} H_C P_n \right) + \text{h.c.} \\
&= \frac{ie}{\hbar A} [\boldsymbol{R}, \bar{H}_C]
\end{aligned}
\tag{S37}
$$

where subleading terms are dropped and $\boldsymbol{R} = \sum_i^N \boldsymbol{R}_i$ is the guiding center coordinate. Since our focus is FCIs, we assume the ground state is insulating; hence the Drude weight vanishes and we can write $W = \int d\omega \, \mathrm{Re} \, \sigma_{aa}^L(\omega)$ as follows [57]

$$
\begin{aligned}
W &= \frac{\pi A}{\hbar} \sum_{n\neq0} \frac{\langle 0|j_a|n\rangle\langle n|j_a|0\rangle}{\omega_{n0}} \\
&= \frac{\pi A}{\hbar} \sum_{n\neq0} \frac{\langle \bar{0}|\bar{j}_a|\bar{n}\rangle\langle \bar{n}|\bar{j}_a|\bar{0}\rangle}{\omega_{n0}} \\
&= \frac{\pi e^2}{2\hbar^2 A} \langle \bar{0}|[R_a, [\bar{H}_C, R_a]]|\bar{0}\rangle \\
&= \frac{\pi e^2}{2\hbar^2 A} \lim_{q\to0} \frac{1}{q^2} \langle \bar{0}|[\bar{\rho}_{\boldsymbol{q}}^\dagger, [\bar{H}_C, \bar{\rho}_{\boldsymbol{q}}]]|\bar{0}\rangle
\end{aligned}
\tag{S38}
$$

where $\boldsymbol{q} = q\hat{a}$. This is in agreement with Eq. (14) of the main text, and Eq. (17) follows.

Optical conductivity in periodically modulated Landau levels

Due to Kohn's theorem, all intra-LL excitations of any state in Landau levels are optically inactive and cannot be probed by optical absorption due to Galilean invariance. To go beyond this, we consider perturbing the Landau level system by adding a periodic potential. As discussed in the main text, the Hamiltonian projected to the lowest Landau level is given by

$$
H = \sum_{\boldsymbol{G}} V_{\boldsymbol{G}} \bar{\rho}_{\boldsymbol{G}} + \frac{1}{2} \sum_{\boldsymbol{q}} U(\boldsymbol{q}) : \bar{\rho}_{\boldsymbol{q}}^\dagger \bar{\rho}_{\boldsymbol{q}} :
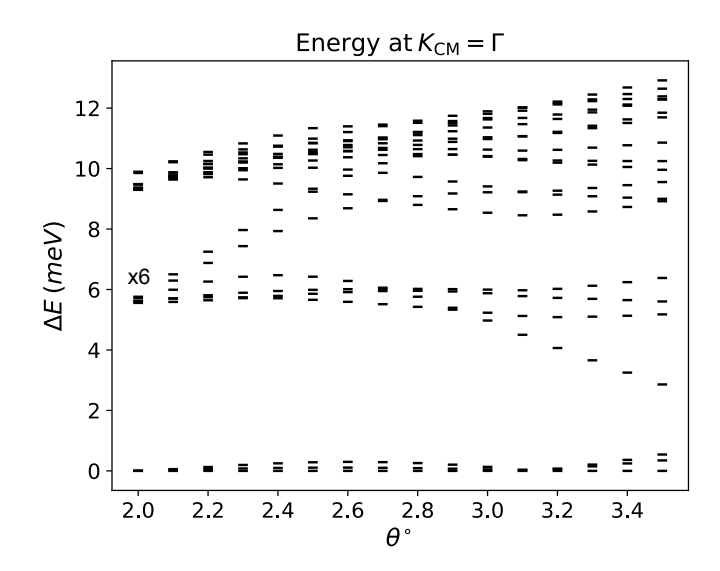\tag{S39}
$$

FIG. S3. Many-body spectrum in the total momentum sector $K_{CM} = 0$ as a function of twist angle calculated for twisted MoTe$_2$ at hole filling $n = 2/3$. There are 3 quasi-degenerate FCI ground states, above which, there exists low-lying collective modes which we argue that they are fractional excitons based on the LL analogy.

We consider a D_6-symmetric potential with six harmonics ($V_{\boldsymbol{G}} = -V_0$ for $\boldsymbol{G}_i = \frac{4\pi}{\sqrt{3}a_0}[\cos 2\pi(i-1)/3, \sin 2\pi(i-1)/3]$ for $i = 1, \ldots, 6$) and a period a_0 chosen such that the unit cell encloses one flux quantum ($\sqrt{3}a_0^2 = 4\pi\ell_B^2$). The periodic potential will broaden the LLL to dispersive Chern band. Due to the periodic potential, continuous magnetic translation symmetry is broken to a discrete one and we can only label the many-body states with momentum quantum number $\boldsymbol{K}_{CM} \in BZ_{Bloch}$. As shown in the many-body spectrum at $\nu = 1/3$ in Fig. S2(a), the periodic potential splits the previously degenerate many-body states (Fig. S1(b)) but the system still in the FCI phase. Above the many-body ground states at $\boldsymbol{K}_{CM} = 0$, we observe low-lying fractional excitons that hybridize and split in energy due to the periodic potential. Next, we calculate the response of the system to left/right circularly polarized light

$$\sigma_{\pm}^{GS}(\omega) = \pi A \sum_{n \neq GS} \frac{|\langle GS|j_{\pm}|n\rangle|^2}{E_n - E_{GS}} [\delta(\omega - (E_n - E_{GS})) + \delta(\omega + (E_n - E_{GS}))] \tag{S40}$$

where $j_{\pm} = (j_x \pm j_y)/\sqrt{2}$ with the current density operator given by $\boldsymbol{j} = \frac{1}{A}\sum_j ie[\boldsymbol{R}_j, V(\boldsymbol{R}_j)]$ with $\boldsymbol{R}_j$ is the guiding center operator for the j-th particle and $V(\boldsymbol{R}) = \sum_{\boldsymbol{G}} V_{\boldsymbol{G}} e^{-|\boldsymbol{G}|^2\ell_B^2/4} e^{-i\boldsymbol{G}\cdot\boldsymbol{R}}$. A is the area of the system. $\sigma_{\pm}^{GS}(\omega)$ (and any response function) can be calculated efficiently using the Lanczos algorithm without the need to find all eigenstates of the system as we explain in a later section.

In Fig. S2(b), we plot $\sigma_{\pm}^{GS}(\omega)$ for the three quasi-degenerate ground states. We find the conductivity to exhibit peaks at frequencies that correspond to the low-lying fractional excitons directly showing that they are optically active (in contrast to the FQH case without any periodic potential).

In addition, we observe in Fig. S2(b) peaks in the higher frequency range ($0.3 < \omega < 0.4$) that correspond to chiral graviton excitations [38, 39] (the $\boldsymbol{q} \to 0$ of the magneto-roton branch, shown Fig. S1(a)). These shows that some of the chiral graviton modes can be optically active when a periodic potential is added. Indeed with a C_n symmetric potential, angular momentum is defined only modulo n and in principle, dipole matrix elements can be non-zero. We leave the detailed study of the optical response of these modes to future work.

Fractional excitons in twisted TMDs

In this section, we study the low-lying collective modes of twisted MoTe$_2$ in the many-body ground state. We use a 27 site cluster [58] for which the quasi-degenerate FCI ground states at $n = 2/3$ occur at Γ (total momentum $K_{CM} = 0$). In Fig. S3, we show the many-body spectrum in this momentum sector as a function of twist angle.

First, we focus at $\theta = 2.0°$ where the system is the closest to the Landau-level limit [15]. At this *magic angle*, we observe 6 low-lying states. Based on the Landau level analogy explained in Fig. S1 for the 27-site cluster, there are
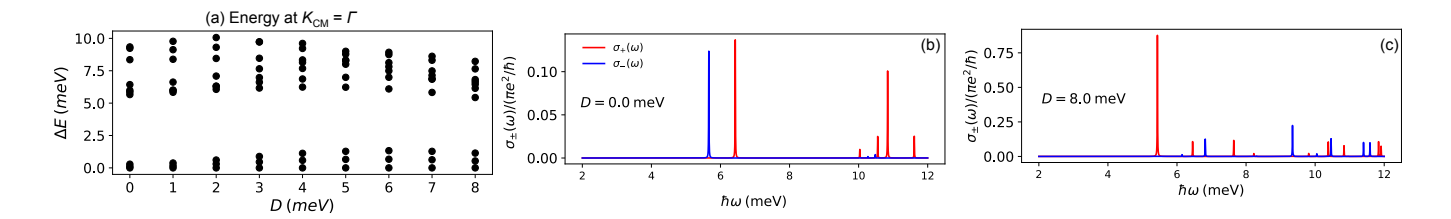
FIG. S4. (a) Many-body energy spectrum of twisted MoTe$_2$ at $n = 2/3$ at Γ ($K_{\mathrm{CM}} = 0$ total momentum sector) as a function of displacement field D at $\theta = 2.5°$. There are three quasi-degenerate FCI ground states states and low-lying collective modes. (b-c) Optical conductivity in the lowest many-body ground state for left (σ^+) and right (σ^-) circularly polarized light at (b) $D = 0.0$ and (c) $D = 8.0$ meV. An artificial broadening of $\eta = 0.01$ meV was used.

six low-lying states in the FQH spectrum at two wavevectors $\boldsymbol{G}_1$ and $-\boldsymbol{G}_1$ that fold back to Γ. The observed states at $\theta = 2.0°$ are in agreement with this physical picture therefore they represent fractional excitons states consisting of quasi-hole and quasi-electron pair separated by a large distance. As a function of twist angle, the six fractional exciton states split in energy but importantly, some of them remain isolated below the continuum at all twist angles.

Optical conductivity in twisted TMDs

Having shown in the previous section that the low-lying collective modes of twisted MoTe$_2$ are fractional excitons, we now study the optical response of these modes. The optical conductivity for left/circularly polarized light is given by equation (S40) where the current density operator in our case is given by $j_\alpha = \dfrac{e^2 \hbar k_\alpha}{m_* A} \sigma_0$ where $\alpha = x, y$ and σ_0 is identity matrix in layer space (see equation (1) in the main text).

In Fig. S4(b-c), we calculate the optical conductivity at $\theta = 2.5°$ for displacement field $D = 0.0$ mev and $D = 8.0$ meV. We observe peaks at frequencies corresponding to the low-lying fractional exciton states (Fig. S4(a)). This provides a proof of principle that these modes are also optically active similar to the case of periodically modulated Landau levels.

Low-frequency optical absorption in twisted TMDs

In this section, we provide more additional data for the oscillator strength $F(\boldsymbol{q})$ (Equation (16) in the main text) in Fig. S6 and the low-frequency optical absorption W (Equation (15) in the main text) in Fig. S5 for twisted MoTe$_2$ at different twist angles. As shown, we find non-zero intraband optical absorption at various twist angles. As discussed in the main text, the intraband optical absorption spectrum is governed by the collective excitations (e.g fractional excitons) of the FCI ground states.

We finally remark that due to the finite number of momentum points (Fig. S6), there is uncertainty in the value of the intraband absorption W due to the fitting error. In our analysis, we find that the data is best fit to a quadratic and quartic function in order to capture the small $\boldsymbol{q}$ features.
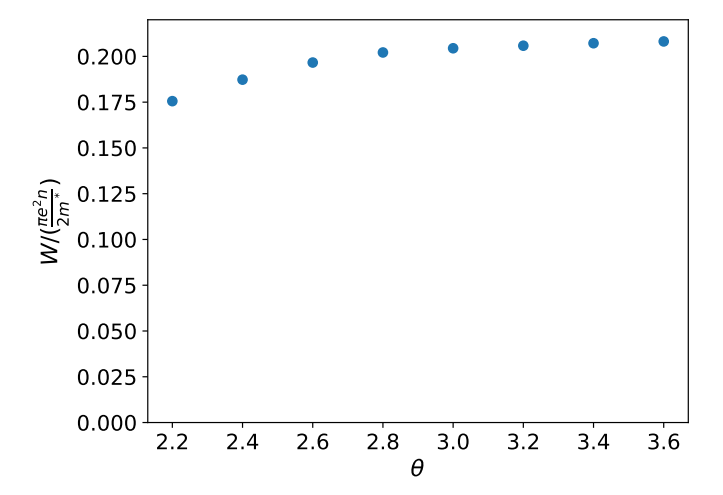
FIG. S5. Total intra-band optical absorption W (equation (15) in the main text) as a function of twist angle for twisted MoTe$_2$ at $n = 2/3$ and zero displacement field.
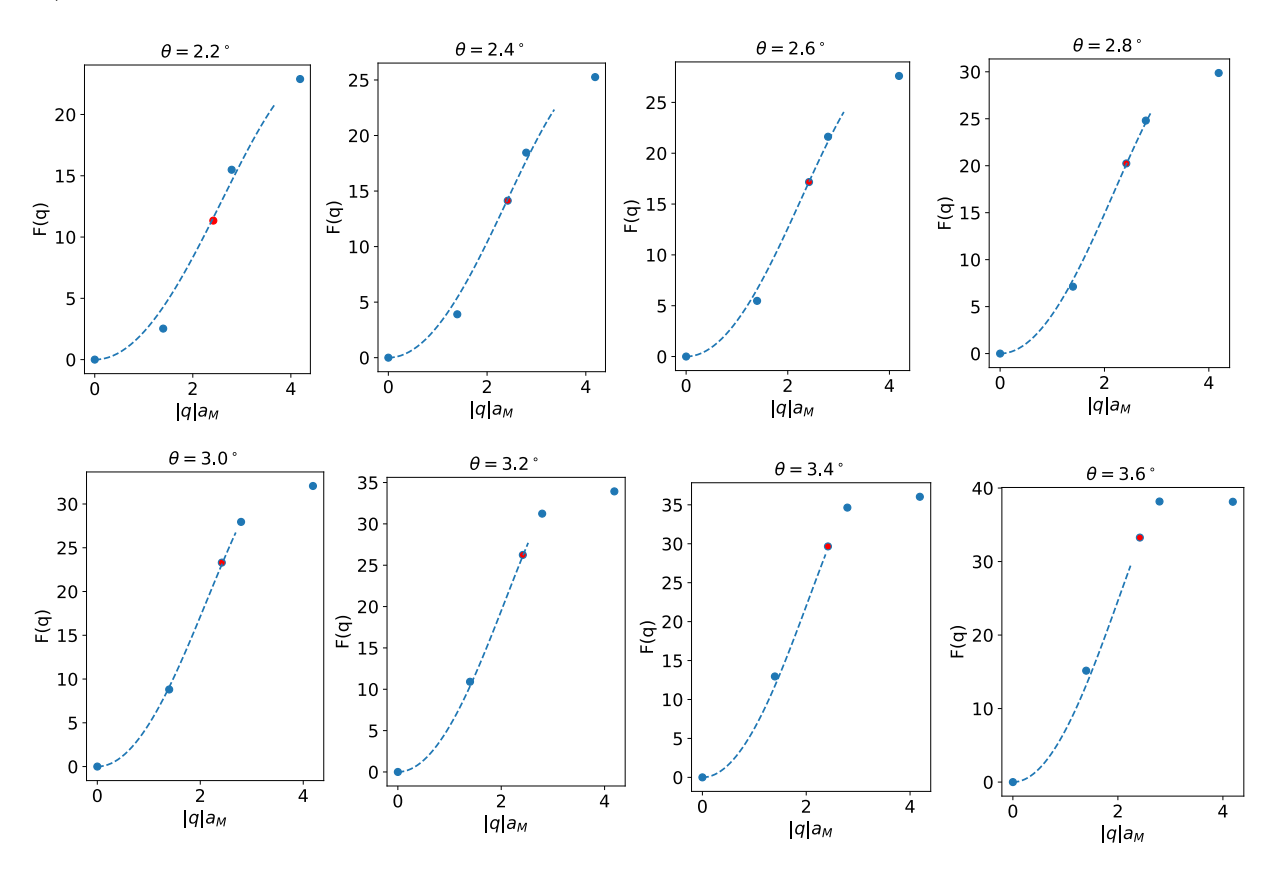

FIG. S6. $F(\boldsymbol{q})$ (equation (16) in the main text) calculated for various twist angles for twisted MoTe$_2$ at $n = 2/3$ and zero displacement field. The data is fitted to a function of the form $F(\boldsymbol{q}) = c_1|\boldsymbol{q}|^2 + c_2|\boldsymbol{q}|^4$. The coefficient c_1 is then extracted to calculated W (equation (15) in the main text) shown in Fig. S5. Refer to the inset of Fig. 2(a) in the main text for the cut used in the momenentum grid.

Numerical Evaluation of Response Functions

In this section, we discuss efficient numerical methods to evaluate arbitrary response functions in frequency space.

(a) Dynamical Response Functions

Quite often, we are interested in evaluating a dynamical response function

$$I_B(\omega) = \sum_{n \neq 0} |\langle 0|B|n\rangle|^2 \delta(\omega - (E_n - E_0)) \tag{S41}$$

where $|0\rangle$ is the many-body state of interest (for example the ground state of a many-body Hamiltonian) with energy E_0 and $|n\rangle$ is the n-th eigenstate of the Hamiltonian with energy E_n. B denotes the response operator (for example current or density). Let's define the Green's function $G_B(Z)$,

$$G_B(Z) = \langle 0|\frac{B^\dagger B}{Z - H}|0\rangle \tag{S42}$$

Equation (S41) can be recast in the following form

$$I_B(\omega) = -\frac{1}{\pi}\lim_{\eta \to 0} \text{Im}\, G_B(\omega + E_0 + i\eta) \tag{S43}$$

where we have made use of the identity $\lim_{\eta \to 0} 1/(\omega \pm i\eta) = \mathcal{P}(1/\omega) \mp 2\pi i\delta(\omega)$ with $\mathcal{P}$ denoting the principal part. A finite η corresponds to broadening the imaginary part from a delta function to a Lorenzian. To evaluate equation (S41) or equation (S43), one can simply find all the eigenstates of the Hamiltonian. However, this is only possible for small systems. As shown in [59], the dynamical correlation function (S43) can be evaluated efficiently in the Krylov subspace of the normalized state $|B\rangle = B|0\rangle/\sqrt{\langle 0|B^\dagger B|0\rangle}$ defined as,

$$\mathcal{K}^L(B) = \text{span}(|B\rangle, H|B\rangle, \ldots, H^L|B\rangle) \tag{S44}$$

This is the same idea behind the standard Lanczos algorithm for finding extremal eigenvalues of a matrix. The orthonormal basis $|v_n\rangle$ in L-th dimensional Krylov subspace $\mathcal{K}^L(B)$ are given by

$$\begin{aligned}
|v_0\rangle &= |B\rangle \\
H|v_n\rangle &= b_n|v_{n-1}\rangle + a_n|v_n\rangle + b_{n+1}|v_{n+1}\rangle \\
a_n &= \langle v_n|H_n|v_n\rangle, \; b_{n+1} = ||H|v_n\rangle - a_n|v_n\rangle - b_n|v_{n-1}\rangle||, \; b_0 = 0
\end{aligned} \tag{S45}$$

The Hamiltonian expressed in this basis takes the form of a tridiagonal matrix,

$$H = \begin{pmatrix}
a_0 & b_1 & 0 & 0 & & 0 & 0 \\
b_1 & a_1 & b_2 & 0 & \cdots & 0 & 0 \\
0 & b_2 & a_2 & b_3 & & 0 & 0 \\
0 & 0 & b_3 & a_3 & & 0 & 0 \\
& \vdots & & & \ddots & & \vdots \\
0 & 0 & 0 & 0 & & a_{L-1} & b_L \\
0 & 0 & 0 & 0 & \cdots & b_L & a_L
\end{pmatrix} \tag{S46}$$

In the Krylov subspace basis (S45), the Green's function (S42) is given by

$$G_B(Z) = \langle 0|B^\dagger B|0\rangle [(Z - H)^{-1}]_{00} \tag{S47}$$

where 00 denote the element of the first row and first column. We then evaluate the inverse of $(Z - H)^{-1}$ by partitioning it into a block 2×2 matrix,

$$Z - H = \begin{pmatrix} Z - a_0 & (B^{(1)})^T \\ B^{(1)} & Z - H^{(1)} \end{pmatrix}$$

$$[(Z - H)^{-1}]_{00} = (Z - a_0 - b_1^2[(Z - H^{(1)})^{-1}]_{00})^{-1} \tag{S48}$$

Evaluating the inverse recursively, we arrive at a continued fraction expression for $G_B(Z)$,

$$\begin{aligned}
G_B(Z) &= \langle 0|B^\dagger B|0\rangle [(Z - H)^{-1}]_{00} \\
&= \cfrac{\langle 0|B^\dagger B|0\rangle}{Z - a_0 - \cfrac{b_1^2}{Z - a_1 - \cfrac{b_2^2}{Z - a_2 - \ldots}}}
\end{aligned} \tag{S49}$$

To evaluate $G_B(Z)$ in the many-body state $|0\rangle$, we first calculate $|A\rangle = B|0\rangle/\sqrt{\langle 0|B^\dagger B|0\rangle}$ then apply L Lanczos iterations as given in (S45) then we evaluate $G_B(Z)$ using equation (S49). The dynamical response function $I_A(\omega)$ can be calculated simply through equation (S43). The number of Lanczos iterations L is increased until convergence is reached. Therefore through this approach, we only need the Hamiltonian H, the state $|0\rangle$ and the response operator B.

Example: Optical Conductivity

We apply this method to calculate the regular part of the optical conductivity which we copy below,

$$\sigma_\pm(\omega) = \frac{\pi A}{|\omega|} \sum_{n \neq 0} |\langle 0|j_\pm|n\rangle|^2 [\delta(w - E_n + E_0) - \delta(w + E_n - E_0)] \tag{S50}$$

With $j_\pm$ the current operator for left/right circular polarization In this case, we take $B = j_\pm$ giving rise to

$$\sigma_\pm(\omega > 0) = -\frac{\pi A}{|\omega|} \frac{1}{\pi} \lim_{\eta \to 0} \operatorname{Im} G_{j_\pm}(\omega + E_0 + i\eta)$$
$$\sigma_\pm(\omega < 0) = -\frac{\pi A}{|\omega|} \frac{1}{\pi} \lim_{\eta \to 0} \operatorname{Im} G_{j_\pm}(\omega - E_0 + i\eta) \tag{S51}$$

From $\sigma_\pm(\omega)$, one can readily compute the real part of longitudinal conductivity $\operatorname{Re}\sigma_{xx}$ or the imaginary part of the Hall conductivity $\operatorname{Im}\sigma_{xy}$ by taking the sum or difference of σ_+ and σ_-.